LIFE SCIENCES

Loss of histone macroH2A1.1 causes kidney abnormalities secondary to a change in nutrient metabolization

René Winkler[1], Gemma Comas-Armangué[2,3], David Corujo[1], Adrián Sanz-Moreno[2], Julia Calzada-Wack[2], Shubhra Ashish Bhattacharya[1,4], Birgit Rathkolb[2,3,5], Nathalia Romanelli Vicente Dragano[2,3], Colina X. Qiao[6], Valentina Chiodi[7], Dan Filipescu[8], Dylan H. Park[6], Maria Rosaria Domenici[7], Valentina Kirigin Callaú[8], Raffaele Gerlini[2], Jan Rozman[2]†, Tanja Klein-Rodewald[2], Antonio Aguilar-Pimentel[2], Lore Becker[2], Claudia Seisenberger[2], Susan Marschall[2], Helmut Fuchs[2], Valérie Gailus-Durner[2], Emily Bernstein[8], Manlio Vinciguerra[9,10], Philipp Oberdoerffer[6], Martin Hrabě de Angelis[2,3,11]*, Raffaele Teperino[2,3]*, Marcus Buschbeck[1,12]*

Histone variants with metabolite-binding macrodomains provide a poorly understood link between chromatin composition and metabolism. To address their contribution to physiological health, we generated and analyzed mice individually lacking the histone variants macroH2A1.1, macroH2A1.2, or macroH2A2. We identified several histopathologic changes in the kidney as isoform-specific phenotype of complete macroH2A1.1 loss affecting male and female animals. Kidney alterations were barely associated with organ-intrinsic gene expression changes but strongly correlated with a systemic shift in nutrient metabolization and alterations in NAD^+ (nicotinamide adenine dinucleotide, oxidized form) metabolism. Reduced lipid oxidation and increased glycolysis were found in male and female mice lacking macroH2A1.1 but not macroH2A1.2 or macroH2A2. Male macroH2A1.1-deficient mice also had better glucose tolerance and altered hepatic gene expression. Replacing chow by ketogenic diet overrode the macroH2A1.1-dependent metabolic phenotype and prevented kidney abnormalities. Together, our results indicate that macroH2A1.1 controls nutrient metabolization and links macroH2A1.1 levels to secondary changes in the kidney.

INTRODUCTION

The genome is stored in the nucleus in the form of chromatin (*1*). The structural unit of chromatin is the nucleosome, which is composed of DNA wrapped around a core of histone proteins (*2*). The existence of histones with metabolite-binding macrodomains provides a poorly understood but direct link between metabolism and chromatin. Macrodomains are ancient protein folds that can bind and, in some cases, metabolize adenosine diphosphate (ADP)–ribose subunits or conjugates (*3*). The fusion of genes encoding an H2A histone fold and a macrodomain occurred at the beginning of animal multicellular life and gave rise to macroH2A proteins (*4*, *5*). The evolution of vertebrates and mammals led to the appearance of a second macroH2A-encoding gene and an alternatively spliced exon (*6*). As a consequence in mammals, macroH2A proteins form a family of three histone variants that can replace replication-coupled H2A in a fraction of nucleosomes (*7*). In many cell types, this fraction corresponds to 1 to 2% of all nucleosomes (*8*). MacroH2As have a tripartite structure in which an unstructured linker connects the conserved histone-fold with the macrodomain locating it at an accessible position outside of the compact nucleosome (*9*).

The *Macroh2a1* gene (previously *H2afy*) gives rise to macroH2A1.1 and macroH2A1.2, and the *Macroh2a2* gene (previously *H2afy2*) encodes macroH2A2. Of these, only the macrodomain of the macroH2A1.1 splice variant retains the capacity to bind ADP-ribose (*10*, *11*), although its affinity decreased during evolution (*5*). On the cellular level, two different functions of macroH2A1.1's capacity to bind ADP-ribose are known. First, macroH2A1.1 has been linked to the transcriptional stress response by recruiting the ADP-ribosylated chromatin modifiers SirT7 and poly(ADP-ribose) polymerase 1 (PARP-1) to target genes (*12*–*14*). Second, and independent of transcriptional regulation, high levels of macroH2A1.1 inhibit the enzymatic activity of PARP-1 and lower the nuclear consumption of its substrate nicotinamide adenine dinucleotide (NAD^+) (*15*). Consequently, macroH2A1.1 increases the NAD^+ availability in mitochondria and their metabolic activity including fatty acid oxidation.

In contrast to core histones and several other histone variants, macroH2As are not essential (*7*). *Macroh2a1* knockout (KO) mice,

[1]Program of Applied Epigenetics, Program of Myeloid Neoplasms, Josep Carreras Leukaemia Research Institute (IJC), Campus Can Ruti, Badalona, Spain. [2]Institute of Experimental Genetics and German Mouse Clinic, Helmholtz Zentrum München, Neuherberg, Germany. [3]German Center for Diabetes Research (DZD), Neuherberg, Germany. [4]PhD Program of Cell Biology, Autonomous University of Barcelona, Barcelona, Spain. [5]Institute of Molecular Animal Breeding and Biotechnology, Gene Center, Ludwig-Maximilians-University München, Munich, Germany. [6]Department of Radiation Oncology and Molecular Radiation Sciences, Johns Hopkins University School of Medicine, Baltimore, MD, USA. [7]Istituto Superiore di Sanità, National Centre for Drug Research and Evaluation, 00161 Rome, Italy. [8]Department of Oncological Sciences, Tisch Cancer Institute, Icahn School of Medicine at Mount Sinai, New York, NY, USA. [9]Department of Translational Stem Cell Biology, Research Institute of the Medical University, Varna, Bulgaria. [10]Faculty of Science, Liverpool John Moores University, Liverpool, UK. [11]Chair of Experimental Genetics, TUM School of Life Sciences, Technische Universität München, Freising, Germany. [12]Germans Trias i Pujol Research Institute (IGTP), Badalona, Spain.
*Corresponding author. Email: mbuschbeck@carrerasresearch.org (M.B.); raffaele.teperino@helmholtz-munich.de (R.T.); martin.hrabedeangelis@helmholtz-munich.de (M.H.d.A.)
†Present address: Luxembourg Centre for Systems Biomedicine (LCSB), University of Luxembourg, Esch-sur-Alzette, Luxembourg.

lacking both macroH2A1.1 and macroH2A1.2, displayed no overt developmental defects (*16*, *17*). Mice lacking all three macroH2A proteins are viable and fertile but have reduced body weight (*18*). Two groups reported that *Macroh2a1* KO mice demonstrated changes in glucose tolerance but came to opposing conclusions regarding whether metabolic health was improved or worsened (*16*, *19*). The reported discrepancies are likely related to differences in the chosen diet, housing conditions, genetic background, or the studied sex. A major drawback of all studies on *Macroh2a1* KO is that they do not discriminate between the specific effects of the ADP-ribose binding isoform macroH2A1.1 and the nonbinding isoform macroH2A1.2. Whether metabolic parameters are altered in *Macroh2a2* KO has not been investigated.

To systematically assess the relative contributions of all three macroH2A proteins to physiology and to clarify a potential influence on metabolism, we have generated and compared isoform-specific KOs of all three macroH2A proteins by applying highly standardized assay conditions. To reduce the impact of potential confounding factors, we harmonized the genetic background, accounted for sex differences, and used wildtype (WT) littermates from heterozygous crossings as optimal age-, sex-, and environment-matched controls. We identify kidney abnormalities in macroH2A1.1 isoform–specific KO mice associated with changes in nutrient metabolization. We further demonstrate that the metabolic and kidney phenotype of macroH2A1.1 KO mice can be rescued with a dietary intervention.

RESULTS

Loss of macroH2A1.1 causes kidney alterations in an isoform-specific manner

To gain insights into the isoform-specific functions of macroH2A histone variants in vivo, isoform-specific KO mouse models were generated and analyzed under highly standardized assay conditions (fig. S1A and table S1). To generate macroH2A1.1 KO and macroH2A1.2 KO mice, we used a previously described mouse strain in combination with a Cre or Dre recombinase (*20*, *21*). MacroH2A2 KO mice were generated using CRISPR-Cas9 technology (Fig. 1A). All KOs were confirmed by Western blot (Fig. 1B). We systematically screened a total of 25 organs for histopathologic changes in the generated mice at the age of 19 weeks (fig. S1B). The only organ with consistent histopathologic alterations between both sexes was the kidney, and we detected abnormalities in 50% of all analyzed macroH2A1.1 KO mice (Fig. 1C and table S2). These atypical findings were primarily the presence of inflammatory interstitial infiltrates in 40% of kidneys that indicate the recruitment of innate or adaptive immune cells (*22*). The infiltrates were composed of CD3-positive cells as shown by further immunohistochemistry approaches (fig. S2A). In addition, we observed one case of a renal infarct out of five analyzed male macroH2A1.1 KO mice, which is rare in mice of that age. Notably, renal infarcts can cause acute kidney injury (*23*). Kidneys of WT, macroH2A1.2 KO, and macroH2A2 KO mice appeared healthy (Fig. 1C). Moreover, we observed an elevated number of hyaline protein aggregates (casts) in hematoxylin and eosin (H&E)–stained sections of kidneys from male and female macroH2A1.1 KO mice (Fig. 1D). Such hyaline casts are formed by precipitation of Tamm-Horsfall protein (uromodulin) due to decreased urine flow, tubular injury, or glomerular injury and can be signs of chronic progressive nephropathy or acute damage (*24*–*27*). We confirmed the proteinaceous origin of the casts (fig. S2B). Notably, the kidneys from female macroH2A1.2 KO mice also showed higher numbers of kidney casts despite an otherwise healthy appearance (Fig. 1D). Mice deficient for macroH2A2 showed no cast accumulation at an age of 16 weeks (Fig. 1D). To exclude that the observed kidney casts in macroH2A1.1 KO mice were due to background or breeding side effects, we investigated another cohort of macroH2A1.1 KO mice that were generated using a different strategy and from a mixed C57BL/6-129S1/Sv background as described before (*28*). Kidneys from these macroH2A1.1 KO mice also displayed an elevated number of kidney casts (Fig. 1E). Moreover, we found a clear correlation between the average number of kidney casts and age, with significantly higher cast accumulation in macroH2A1.1 KO mice with C57BL/6J background (Fig. 1F). An aged cohort of macroH2A2 KO mice (78 weeks old) also displayed more casts than young animals, but no difference to WT mice was found (fig. S2C). Last, to exclude that deregulation of other macrohistone variants caused the development of kidney casts, we analyzed kidneys from macroH2A1.2/macroH2A2 double-knockout (DKO) mice with mixed C57BL/6-129S1/Sv background (Fig. 1G). These mice phenocopied isoform-specific macroH2A1.2 KO regarding the female-specific appearance of kidney casts (Fig. 1D), concluding that the loss of macroH2A1.1 is responsible for the sex-independent formation of kidney casts.

Given that macroH2A1.1 is a chromatin component, we wondered whether these kidney alterations were associated with tissue-intrinsic changes in gene expression. We analyzed kidney tissues from male mice and confirmed the complete absence of macroH2A1.1 transcripts in macroH2A1.1 KO tissue, which was accompanied by a subtle increase in transcripts of its alternative splice variant macroH2A1.2 (Fig. 1H). *Macroh2a2* transcript levels were unaffected and were the lowest expressed isoform in kidney (Fig. 1H and fig. S2D). When analyzing the whole transcriptome, principal components analysis clustered the samples by genotype on the second component explaining only 18% of the variability (fig. S2E). Only 18 genes displayed significant, and, in most cases, subtle, changes in expression (Fig. 1I and fig. S2F). These genes included *Macroh2a1*, which encodes both macroH2A1.1 and macroH2A1.2, underlining that the observed up-regulation of the macroH2A1.2 transcript did not fully compensate for the loss of macroH2A1.1 transcripts. The genes *Sfi1* and *Unc5a* were deregulated in kidneys after loss of macroH2A1.1, which was confirmed by reverse transcription quantitative polymerase chain reaction (RT-qPCR) (Fig. 1J). *SFI1* was shown to be associated with diabetic kidney disease in a human cohort (*29*). *UNC5A*, in contrast, encodes a receptor that binds Netrin-1, which protects from acute kidney disease (*30*). To understand potential implications of kidney casts for kidney function, we correlated the number of observed casts in mice of different ages with known clinical chemistry parameters of impaired kidney function (*31*–*33*). Serum magnesium and creatinine levels as well as serum cystatin C levels correlated significantly with the number of casts (fig. S2G and table S3). Cystatin C is a well-known indicator of kidney damage (*34*), and we checked the expression of the encoding gene *Cst3*, which was significantly increased in macroH2A1.1-deficient kidneys at young age (fig. S2H).

Together, these results show that the kidney abnormalities in the form of elevated numbers of casts are a specific loss-of-function phenotype of the macroH2A1.1 isoform affecting both male and female mice. The absence of major gene expression changes in the kidney suggests that organ-intrinsic transcriptional regulation is not the primary cause of these abnormalities.

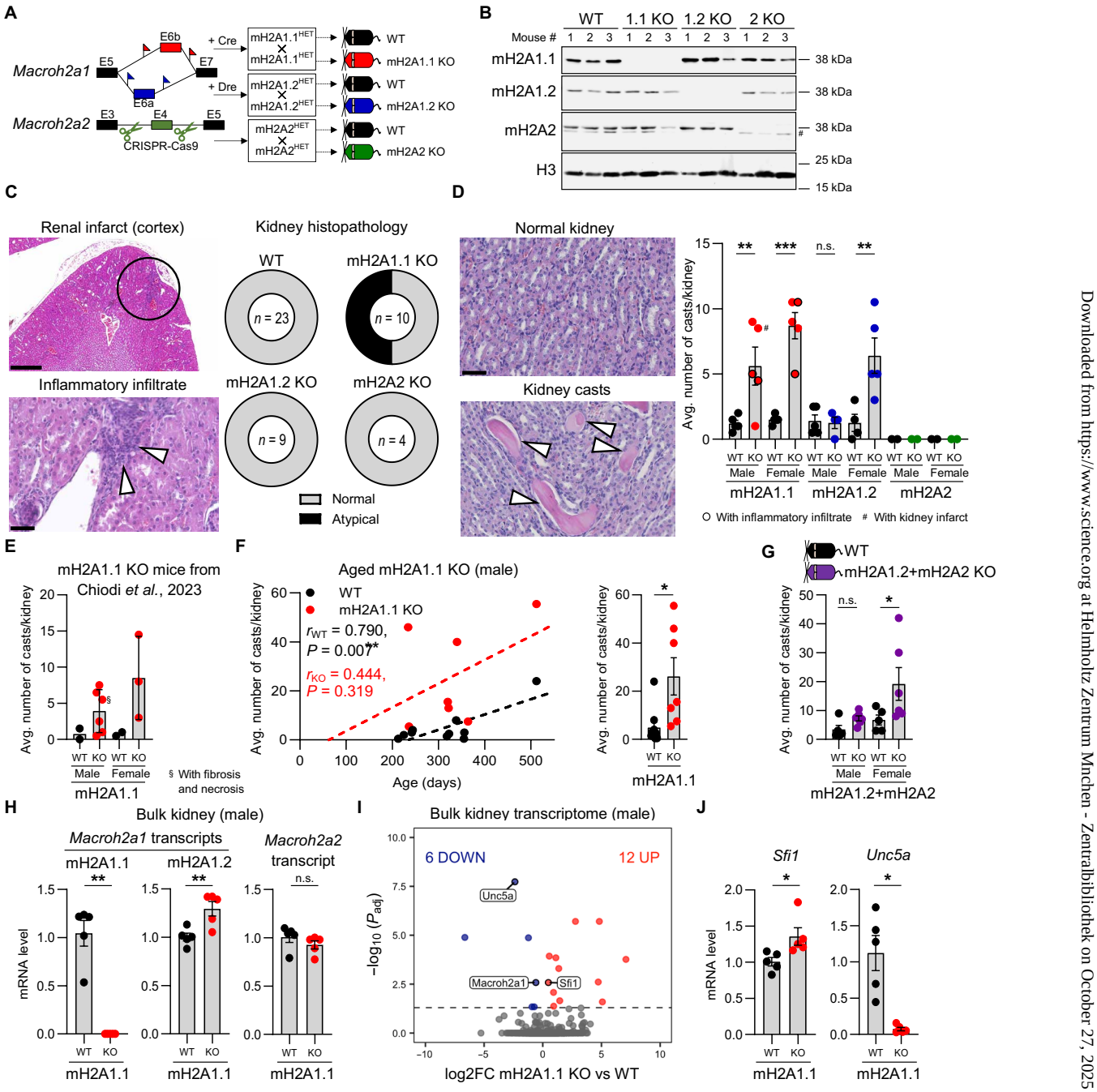

Fig. 1. Loss of macroH2A1.1 provokes histopathologic alterations in the kidneys of mice. (**A**) Scheme showing generation of isoform-specific macroH2A (mH2A) KO mice using different engineering and recombination strategies. Flags indicate loxP/rox sites. HET, heterozygous. (**B**) For isoform-specific KO validation, spleen lysates from three individual mice of each genotype were analyzed by immunoblotting. Histone 3 (H3) served as loading control. # indicates an unspecific band. Blots from different runs were cropped. For all blots, see the Supplementary Materials. (**C**) Images of histopathologic kidney alterations are shown by H&E staining. Bar indicates 500 μm (top) or 50 μm (bottom). Number of affected mice is shown. WT and KO mice of both sexes on a regular chow diet were analyzed at 19 weeks of age. (**D**) Representative H&E staining of sections from normal and cast-bearing inner medulla of kidneys are shown. Bar indicates 50 μm. The mice were between 16 and 20 weeks old. Two-way analysis of variance (ANOVA) with Fisher's least significant difference (LSD). $P_{mH2A1.1male} = 0.003$; $P_{mH2A1.1female} < 0.0001$; $P_{mH2A1.2male} = 0.906$; $P_{mH2A1.2female} = 0.001$. (**E**) Average number of kidney casts in a cohort of mH2A1.1 KO mice (16 weeks old) generated with a different method as described in (*28*). (**F**) Correlation of age and kidney casts in an independent cohort of male mice. Pearson's *r* is displayed with significance. Unpaired Student's *t* test with Welch's correction. $P = 0.033$. (**G**) Kidney casts were analyzed in mH2A1.2/mH2A2 DKO mice (19 weeks old). Two-way ANOVA with Fisher's LSD. $P_{male} = 0.510$; $P_{female} = 0.016$. (**H**) Relative mRNA levels encoding mH2A isoforms were measured in kidney tissue from male mH2A1.1 KO and WT mice by RT-qPCR ($n = 5$). Unpaired Student's *t* test, if necessary, with Welch's correction. $P_{mH2A1.1} = 0.001$; $P_{mH2A1.1} = 0.009$; $P_{mH2A1.1} = 0.282$. (**I**) Bulk RNA sequencing (RNA-seq) from male whole-kidney tissue for $n = 5$ WT and $n = 5$ mH2A1.1 KO. Differentially expressed genes (DEGs) with an adjusted $P < 0.05$ are shown. (**J**) Selected genes related to kidney dysfunction are displayed. $P_{Sfi1} = 0.032$; $P_{Unc5a} = 0.012$. log2FC, log 2 fold change; n.s., not significant.

Loss of macroH2A1.1, but not macroH2A1.2 or macroH2A2, reduces lipid oxidation and increases glucose metabolization in mice fed a chow diet

In cultured muscle and liver cells, the histone variant macroH2A1.1 facilitates oxidative phosphorylation in a strictly isoform-dependent manner (*5*, *15*). As kidneys are a tissue with high metabolic demand (*35*), we hypothesized that an altered metabolism in macroH2A1.1 KO mice might cause the observed kidney abnormalities. We performed a detailed metabolic analysis of all three macroH2A KO mice compared to WT littermates at a young adult age under a standard carbohydrate-rich diet (chow).

Metabolic rates and substrate oxidation were measured by indirect calorimetry in individually caged mice. As shown in Fig. 2A, macroH2A1.1 KO mice had an increased respiratory exchange ratio (RER; Fig. 2A). This reflected reduced lipid (RER = 0.7 for pure lipid oxidation) and an increased carbohydrate (RER = 1.2 for pure carbohydrate oxidation) oxidation (fig. S3, A and B). MacroH2A1.2 KO mice showed the opposite effects and a reduced RER (Fig. 2A and fig. S3, A and B). No differences in RER were observed for macroH2A2 KO mice when compared to controls. As changes were more pronounced in the second half of the dark phase, we separately analyzed the early dark [18:00 to 00:00 Central European Time (CET)] and late dark phase (00:00 to 06:00 CET) in our statistical analysis. The mean RER of macroH2A1.1 KO was increased during the second part of the night, where most mean RER values were close to 1.0, indicating pure metabolization of carbohydrates and an absence of lipid oxidation, reminiscent of a systemic Warburg-like effect (Fig. 2B; fig. S3, A and B; and table S4). This peak in RER during the late phase of the night coincided with higher food intake (fig. S3C).

Although macroH2A1.1 KO mice were hyperphagic (Fig. 2C), the increased food intake had no significant effect on the body weight (Fig. 2D), indicating an energy leak. Energy expenditure judged on the levels of metabolic rate (fig. S4A) and physical activity (fig. S4B) was unchanged in macroH2A1.1 KO mice compared to their WT controls. We observed subtle sex- and genotype-dependent changes in relative lean and fat mass of the different KO mouse models, but nothing correlated consistently with the observed sex-independent changes in RER (fig. S4, C and D).

Together, our observations indicate that macroH2A1.1 is the only macroH2A isoform reducing lipid oxidization and increasing glucose metabolization in both male and female mice. This matches previous observations made in cell culture experiments showing that macroH2A1.1 loss limited the capacity of mitochondria to oxidize fatty acids (*15*).

MacroH2A1.1 loss-dependent metabolic alterations are associated with increased glucose tolerance and changes in the hepatic expression of metabolic genes

To gain a broader picture of the macroH2A1.1-specific metabolic changes, we analyzed glucose metabolism and liver function. We did not detect differences in steady-state glucose levels in peripheral blood under ad libitum conditions in any macroH2A KO mice compared to the respective WT controls (fig. S5A). We then decided to measure glucose tolerance by intraperitoneal injection of glucose in mice that were fasted for 6 hours, and male but not female macroH2A1.1 KO mice had a better glucose tolerance compared to their WT littermates (Fig. 3A and fig. S5B). To quantify the dynamics in blood glucose for individual animals, we calculated the area under the curve (AUC) for two different periods. The initial rise occurring during the first 30 min is indicative of early insulin-induced glucose absorption, while the decline during the subsequent 90 min captures the late insulin response. Male macroH2A1.1 KO mice showed a lower peak after glucose injection indicating better glucose tolerance, while male macroH2A1.2 KO declined faster to baseline levels (Fig. 3B). However, we did not detect altered insulin levels in steady state or after fasting in macroH2A1.1 KO or macroH2A1.2 KO mice when compared to controls (fig. S5C). Furthermore, we did not observe differences in glucose dynamics in male macroH2A2 KO mice or female mice of any genotype (Fig. 3B).

We next analyzed liver function and gene expression in male macroH2A1.1 KO mice, as the substrate utilization and glucose tolerance were altered compared to controls. First, we examined the expression of all macroH2A isoforms in liver tissue to check for possible compensatory mechanisms. We were able to confirm the absence of macroH2A1.1 transcripts and found no alterations in the levels of macroH2A1.2 or *Macroh2a2* transcripts (Fig. 3C). The detectable levels of liver enzyme activity in plasma from peripheral blood as markers of liver injury and inflammation were unaltered when comparing macroH2A1.1 KO and WT mice (Fig. 3D and fig. S5D). Clinical chemistry measurements showed that non–high-density lipoprotein (non-HDL) cholesterol levels were elevated in male macroH2A1.1 KO mice (Fig. 3E). This was not observed in female mice or for HDL cholesterol (fig. S5, E and F).

To check whether global transcriptome changes were present in macroH2A1.1-deficient livers, we performed RNA sequencing (RNA-seq) of homogenized liver tissue from male WT and macroH2A1.1 KO mice. The genotype separated samples in a principal components analysis despite notable variation between individual animals (fig. S5G). In contrast to the kidney transcriptomes, we identified a higher number of differentially expressed genes (DEGs) when comparing macroH2A1.1 KO liver samples to controls (Fig. 3F and fig. S5H). Of a total of 92 DEGs, 58 were up-regulated and 34 were down-regulated in livers lacking macroH2A1.1. These included genes encoding the intracellular uridine diphosphate–glucose transporter *Slc35d2*, the circadian regulators *Per1* and *Noct*, and the calcium signaling genes *Plcd3*, *Camkk2*, and *Camk2*, as well as *Angptl8* or fatty acid binding protein 5 (*Fabp5*).

To identify deregulated pathways, we performed gene ontology (GO) analysis. We found that GO terms of molecular functions related to the observed metabolic phenotype were among up-regulated but not down-regulated GO terms (Fig. 3G, fig. S5I, and table S5). Clustering by similarity of a total of 32 significantly up-regulated GO terms showed enrichment of pathways related to ion and lipid transport, lipid metabolism including steroid hormone synthesis, and binding of peroxisome proliferator–activated receptor (PPAR), a key transcription factor in lipid metabolism (Fig. 3G). This corresponded to the observed up-regulation of genes related to lipid metabolism, such as *Lpin1* and *Lpin2*, which encode Lipin 1 and Lipin 2, or very-low-density lipoprotein receptor, *Vldlr* (Fig. 3F). We compared our data from murine liver tissue with a recently published dataset of transcriptomics from human HepG2 liver cells lacking all macroH2A isoforms (*36*). The overlap shows that *Vldlr* is commonly up-regulated after the loss of macroH2A1.1 (fig. S5J).

Together, the shift from fat to glucose metabolization in macroH2A1.1 KO mice was accompanied by an increased glucose tolerance in male mice and an up-regulated expression of genes related to lipid metabolism. It is plausible that the latter reflects a compensatory response to the reduced capacity to metabolize lipids.

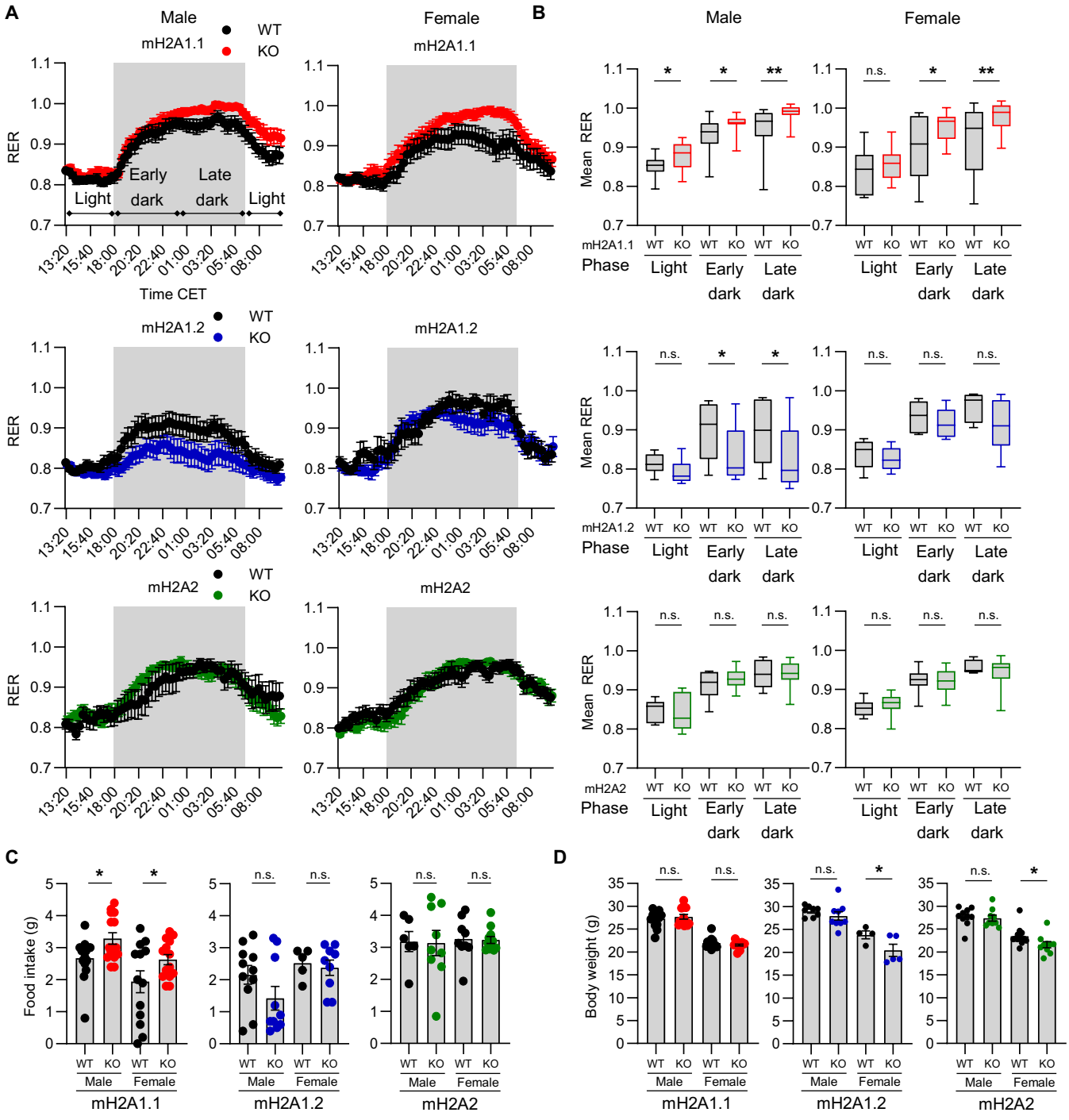

Fig. 2. Loss of the histone variant macroH2A1.1 but not macroH2A1.2 or macroH2A2 reprograms the metabolism toward reduced lipid oxidation. (**A**) RERs were determined for 21 hours every 20 min for young adult WT and age-matched macroH2A (mH2A) isoform-deficient (KO) mice of both sexes (n = 5 to 15 per group). The nighttime is indicated in gray, and the separation into three distinct phases is marked: light (13:00 to 18:00 CET and 06:00 to 10:00 CET), early dark (18:00 to 00:00 CET), and late dark (00:00 to 06:00 CET). Data are plotted as means ± SEM. A full linear mixed model by restricted maximum likelihood was calculated and likelihood ratio test chi-square is given as P. $P_{mH2A1.1}$ = 0.004; $P_{mH2A1.2}$ = 0.029; P_{mH2A2} = 0.886. Full calculation can be found in table S4. (**B**) Comparison of the mean RER between WT or isoform-specific macroH2A KO mice of the three different phases, based on the data shown in (A). Boxes display Q1 and Q3, the median as a band, and minimum to maximum range. P values were calculated by ordinary one-way ANOVA with Fisher's LSD and can be found in the Supplementary Materials. (**C**) Food intake was tracked during RER measurements for each mouse within 21 hours. Data are displayed as means ± SEM. Each dot indicates one individual mouse. P values were calculated by two-way ANOVA with Fisher's LSD and can be found in the Supplementary Materials. RER, respitory exchange ratio. (**D**) Body weights of isoform-specific macroH2A KO and control littermates were determined for 18-week-old mice for the indicated genotypes under standard diet conditions. Data are plotted, and P values were calculated as in (C).

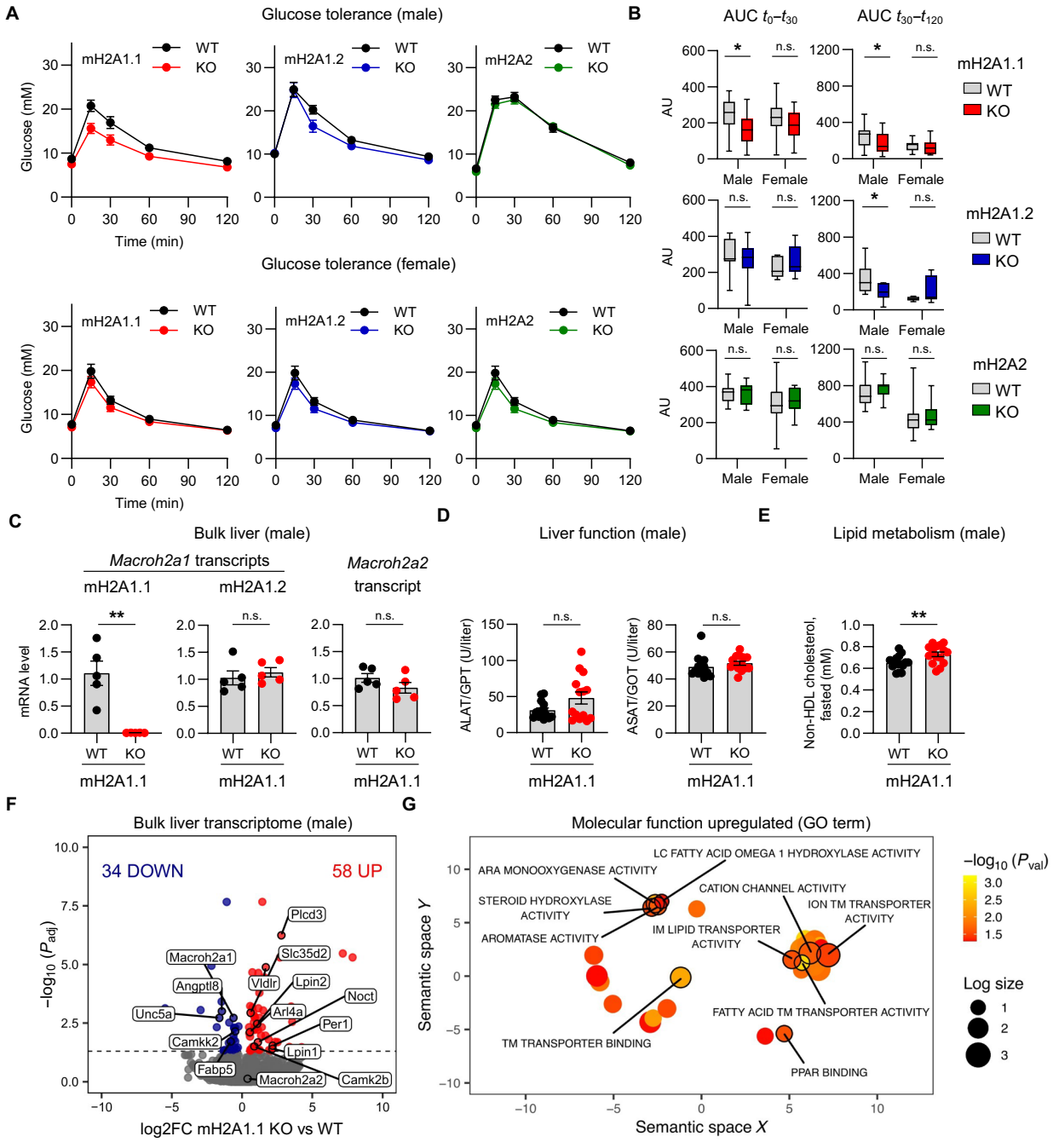

Fig. 3. Male macroH2A1.1 KO mice have better glucose tolerance and altered expression of metabolic genes in the liver. (**A**) An intraperitoneal glucose tolerance test was performed after 6 hours of fasting. Glucose levels were determined in the peripheral blood at indicated time points after intraperitoneal injection of 2 g glucose/kg of body weight. For each genotype, $n \geq 9$ male or $n \geq 5$ female mice were analyzed. (**B**) AUC was calculated for the timespans 0 to 30 min (t_0–t_{30}) and 30 to 120 min (t_{30}–t_{120}). All samples were individually adjusted to their baseline. Arbitrary units (AU) are plotted. *P* values were calculated by two-way ANOVA with Fisher's LSD (see the Supplementary Materials). (**C**) Levels of mRNA encoding macroH2A isoforms were measured in liver tissue from male mice under standard diet conditions by RT-qPCR ($n = 5$ per group). Unpaired Student's *t* test, with Welch's correction if necessary. $P_{mH2A1.1} = 0.008$; $P_{mH2A1.1} = 0.530$; $P_{mH2A1.1} = 0.195$. (**D**) Parameters of liver function were compared in plasma from peripheral blood of male mice under standard diet conditions ($n = 14$ per group): alanine aminotransferase/glutamate pyruvate transaminase (ALAT/GPT) and aspartate aminotransferase/glutamic oxaloacetic transaminase (ASAT/GOT) activity. Unpaired Student's *t* test, with Welch's correction if necessary. $P_{ALAT} = 0.074$; $P_{ASAT} = 0.301$. (**E**) Non-HDL cholesterol levels were calculated from total cholesterol minus HDL cholesterol measured in the plasma of male fasted mice ($n = 15$ per group). Unpaired Student's *t* test, $P = 0.008$. (**F**) RNA-seq was performed on male whole-liver tissue for WT ($n = 4$) and mH2A1.1 KO ($n = 5$). DEGs with an adjusted $P < 0.05$ are shown in the volcano plot. Genes with metabolic relevance are highlighted. (**G**) Gene ontology (GO) analysis was performed on the complete dataset from (F). Significantly up-regulated GO terms of molecular functions ($P < 0.05$) were clustered using the REVIGO tool. ARA, arachidonic acid; IM, intramembrane; LC, long chain; PPAR, peroxisome proliferator–activated receptor; TM, transmembrane.

A ketogenic diet overrides the metabolic defect in macroH2A1.1-deficient mice

The glycolytic phenotype of macroH2A1.1 KO mice was observed under standard chow diet conditions, and we wondered whether the phenotype could be counteracted by a dietary intervention. We have chosen a ketogenic diet (KD) for two reasons: First, its energy content composed of 84% fat, 11% protein, and 5% carbohydrates enforces the utilization of lipids. Second, the metabolization of KD has a reduced requirement for NAD^+ compared to chow diet. Therefore, we fed another cohort of young adult male and female macroH2A1.1 KO and WT mice with a KD starting at the age of 6 weeks (fig. S1A). After 6 weeks of exposure to a KD, phenotyping was started and we observed an increase in the adiposity index, calculated as the ratio of fat mass to lean mass (fig. S6A). Liver steatosis was present at time of sacrifice (19 weeks old), reflected in the accumulation of fat droplets (fig. S6B). At the molecular level leptin, a hormone mostly produced by fat cells was highly increased after KD (fig. S6C). These data demonstrate that KD was effective in male and female WT and macroH2A1.1 KO mice.

We repeated the metabolic measurements for which we had observed differences under chow diet. The RER of male macroH2A1.1 KO mice fed with KD was between 0.7 and 0.8, indicating primarily fat oxidation (Fig. 4A). No difference between macroH2A1.1 KO and WT mice was observed for both sexes (Fig. 4, A and B, and fig. S6, D and E) (full linear mixed model statistics for macroH2A1.1 KO mice under KD: $P = 0.629$; table S4). Food intake, carbohydrate oxidation, and lipid oxidation rates were equal between macroH2A1.1 KO and WT mice under KD (fig. S6, F to H). We further did not detect differences in blood glucose levels of macroH2A1.1 KO mice under KD compared to controls (fig. S6I). As a well-known consequence of prolonged KD, we observed reduced glucose tolerance in all animals comparing those on KD to those on a chow diet (compare Figs. 4C and 3A, and fig. S6J). However, the level of tolerance to glucose was indistinguishable between macroH2A1.1 KO and WT animals in both males and females (Fig. 4D and fig. S6K).

We also checked the expression of a panel of genes that we identified in male mice to be macroH2A1.1-dependent under chow diet

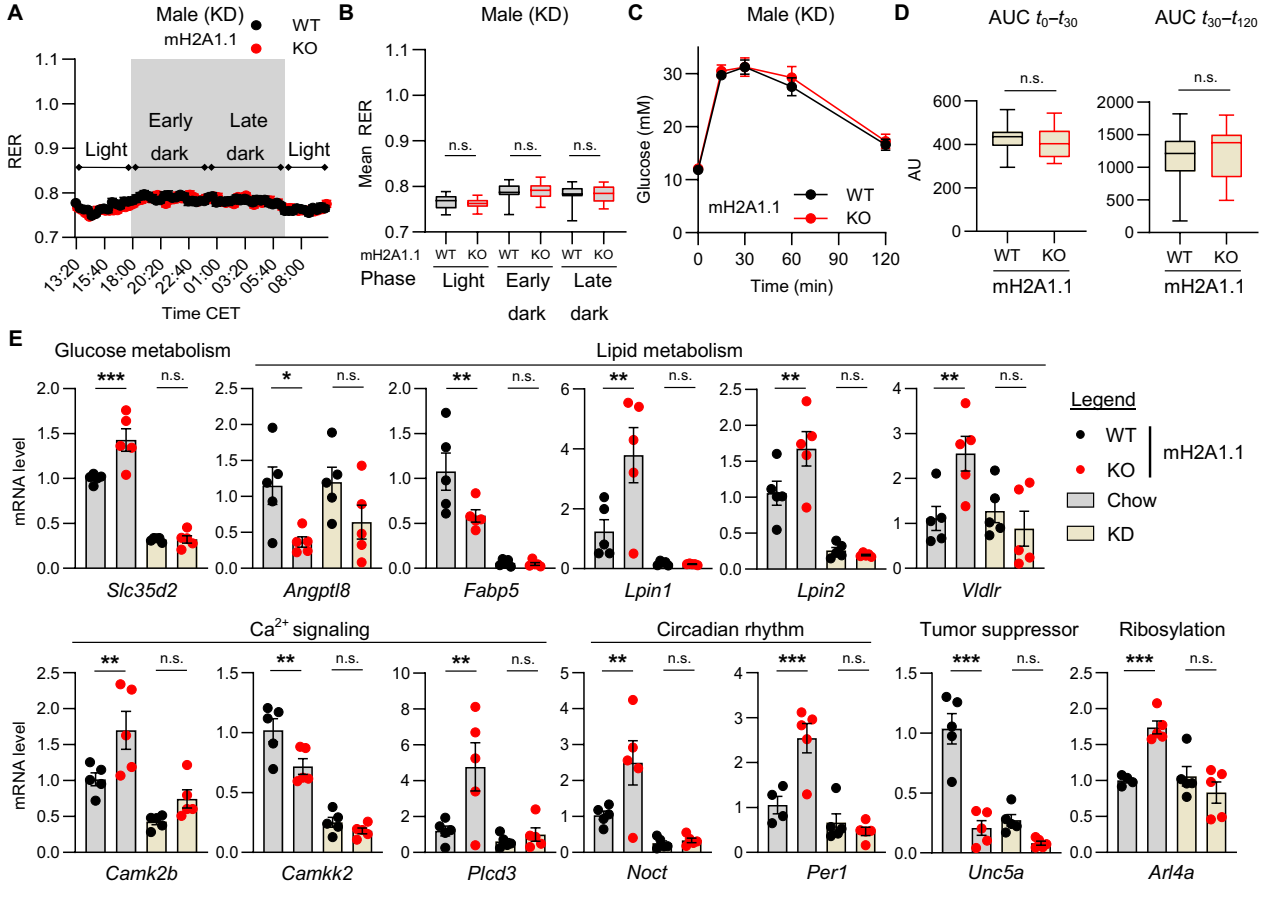

Fig. 4. KD overrides the intrinsic metabolic defect in male macroH2A1.1-deficient mice and blunts differences in hepatic gene expression. (**A**) Male macroH2A1.1 KO and control WT littermates were fed a KD starting at the age of 6 weeks ($n = 15$ per group). RERs were measured at an age of 13 weeks and plotted as in Fig. 2A. (**B**) Comparison of the mean RER between male WT or macroH2A1.1 KO mice under KD of three different phases: light (13:00 to 18:00 CET and 06:00 to 10:00 CET), early dark (18:00 to 00:00 CET), and late dark (00:00 to 06:00 CET) based on the data shown in (A). *P* values were calculated by ordinary one-way ANOVA with Fisher's LSD. $P_{light} = 0.579$; $P_{early} = 0.968$; $P_{late} = 0.971$. (**C**) An intraperitoneal glucose tolerance test was performed as in Fig. 3A for male mice of the indicated genotypes under KD ($n = 15$). (**D**) AUC was calculated as in Fig. 3B. *P* values were calculated using unpaired Student's *t* test. $P_{t0–t30} = 0.696$; $P_{t30–t120} = 0.742$. (**E**) Gene expression of selected genes was measured by RT-qPCR in whole-liver tissue from male mice of both genotypes ($n = 5$ per group) under the indicated diet conditions. Fold induction was normalized to the mean of the corresponding WT samples. Data are displayed as means ± SEM. For *Arl4a* and *Per1*, data from one WT sample were removed as statistical analysis indicated an outlier. *P* values were calculated using ordinary one-way ANOVA with Fisher's LSD (see the Supplementary Materials).

(Fig. 4E). For these, we compared the mRNA levels in livers of male WT and macroH2A1.1 KO mice held under KD conditions with those fed a chow diet. We were able to confirm the changes previously identified by our transcriptomic analysis such as increased expression of *Lpin1*, *Lpin2*, *Slc35d2*, and *Vldlr* (Fig. 4E). KD reduced the overall expression of some genes such as *Lpin1* and *Lpin2* and did not affect others such as *Angptl8* or *Vldlr* in WT mice. Notably, KD also reduced the expression of macroH2A1.1, macroH2A1.2, and, to a lesser extent, macroH2A2 (fig. S6L). All differences in gene expression found between macroH2A1.1-deficient and WT liver tissue under chow diet were lost under KD (Fig. 4E). This was independent of whether genes were up- or down-regulated under chow diet or whether they were sensitive to KD or not.

Together, the metabolic differences between macroH2A1.1-deficient and WT mice in RER, male glucose tolerance, and liver gene expression were lost under a KD diet. We conclude that enforced lipid utilization overrides the intrinsic metabolic alterations of macroH2A1.1 KO mice.

A KD prevents kidney abnormalities in macroH2A1.1 KO mice

The kidney controls water homeostasis by balancing incoming water from drinking and food through urine production and has a high-energy demand (*35*). We hypothesized that the observed kidney abnormalities in macroH2A1.1 KO mice under chow diet could be secondary to their metabolic alterations. From our previous studies in cultured myogenic and hepatic cells, we know that loss of macroH2A1.1 reduces the capacity of energy generation by limiting the availability of NAD^+ outside of the nucleus and in mitochondria (*5*, *15*). One of the reasons we chose KD as a dietary intervention was that the metabolization of ketone bodies requires only one-third of NAD^+ molecules compared to glucose oxidation (*37*).

As KD ablated the genotype-specific metabolic differences between macroH2A1.1 KO and WT mice, we wondered whether kidney tissue integrity and parameters related to water homeostasis changed due to KD. While under the chow diet, half of the macroH2A1.1 KO animals had renal histopathologic abnormalities, and we did not observe these changes in any of the 10 analyzed macroH2A1.1 KO mice on KD (Fig. 5A). Furthermore, the number of proteinaceous casts in the kidneys was reduced in macroH2A1.1 KO mice of both sexes under KD (Fig. 5B). The average number of kidney casts in male macroH2A1.1 KO mice under KD was indistinguishable from WT mice (Fig. 5B).

To characterize the water homeostasis in macroH2A1.1 KO mice, we assessed urination, monitored water intake as well as sodium

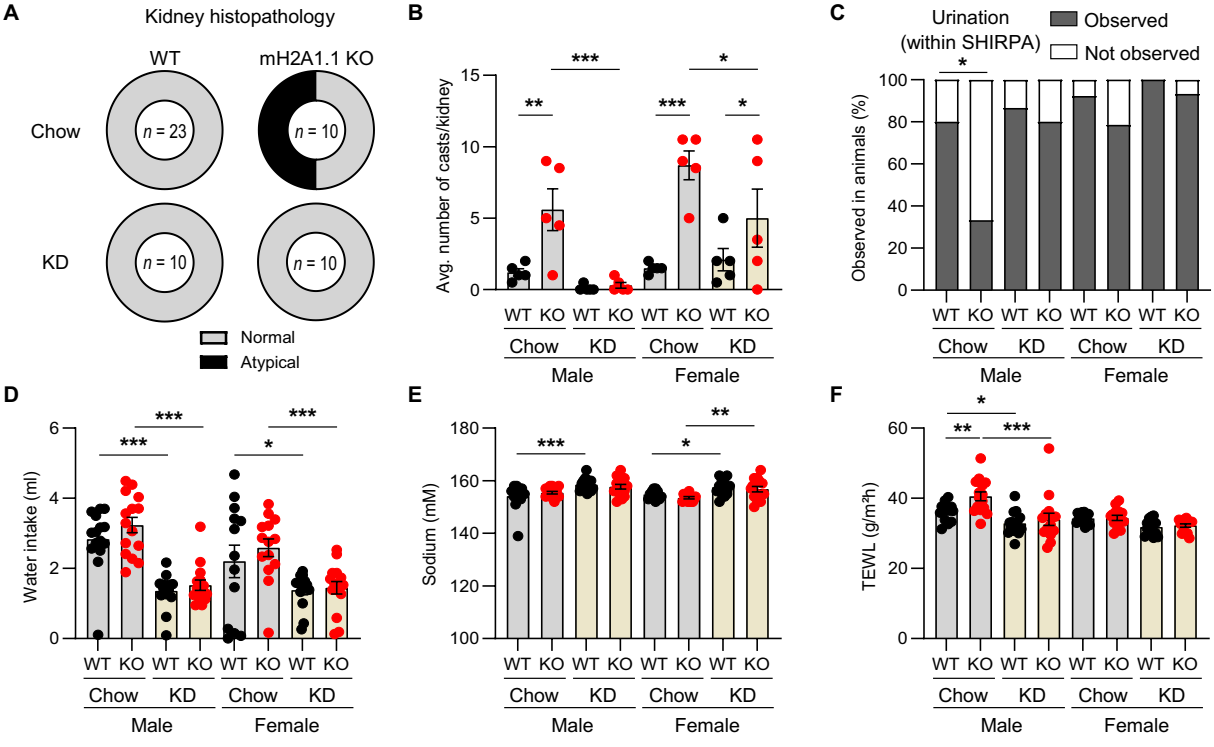

Fig. 5. KD prevents kidney alterations in macroH2A1.1 KO mice. (**A**) After about 3 months of KD, the kidneys of male and female macroH2A1.1 (mH2A1.1) KO ($n = 10$) and WT ($n = 10$) littermates were dissected to assess potential histopathologic alterations. No histopathologic alterations were observed. For reasons of comparison, we include the data from mice on a standard chow diet from Fig. 1C. (**B**) Hematoxylin and eosin (H&E) staining of kidney sections was performed on both kidneys for each sex and genotype ($n = 5$ per group). Casts were counted and averaged. *P* values were calculated using three-way ANOVA with Fisher's LSD (see the Supplementary Materials). (**C**) The presence or absence of urination in male and female mH2A1.1 KO mice and control WT littermates ($n \geq 13$ per group) under chow diet and KD conditions was monitored during 3 min of modified SHIRPA testing. Fisher's exact test was performed for male WT and mH2A1.1 KO mice under chow diet. $P = 0.0253$. (**D**) Water intake of male and female mH2A1.1 KO mice and control WT littermates ($n \geq 13$ per group) under chow diet and KD conditions was tracked over 21 hours. Three-way ANOVA with Fisher's LSD (see the Supplementary Materials). (**E**) Sodium plasma levels were determined using clinical chemistry analysis ($n \geq 13$ per group). Three-way ANOVA with Fisher's LSD (see the Supplementary Materials). (**F**) TEWL was measured on the skin of male and female mH2A1.1 KO mice and control WT littermates ($n \geq 13$ per group) under chow diet and KD conditions. TEWL corresponds to the amount of water lost due to diffusion and evaporation. Three-way ANOVA with Fisher's LSD (see the Supplementary Materials).

levels, and measured transepidermal water loss (TEWL). KD did not affect the urination of WT mice that urinated in 80 to 100% of cases at least once within 3 min (Fig. 5C). However, urination was reduced in male macroH2A1.1 KO mice under a chow diet and returned to normality under KD (Fig. 5C). Water intake, in general, did not depend on the genotype but was reduced under KD in all mice (Fig. 5D). This reduction in water intake during KD was accompanied by an increase in plasma sodium levels (Fig. 5E). We expected that the metabolization of fat generated more so-called metabolic water in the body than carbohydrates, decreasing the need for external water intake. The reduced urination of macroH2A1.1 KO male mice under chow diet was accompanied by an increase in TEWL (Fig. 5F). While the plasma levels of lactate, creatinine, urea, albumin, and total protein remained largely unaffected besides increased serum creatinine in female macroH2A1.1 KO mice across diets (fig. S7, A to E), we noticed a significant decrease in urinary creatinine but not urinary albumin in male macroH2A1.1 KO mice under chow diet (fig. S7F). Notably, KD increased liver damage markers such as alanine aminotransferase/glutamate pyruvate transaminase (ALAT/GPT) and aspartate aminotransferase/glutamic oxaloacetic transaminase (ASAT/GOT) but not alkaline phosphatase (AP) (fig. S7G). Together, these results show that a dietary intervention can rescue kidney integrity and function.

NAD^+ metabolism in the liver and kidney is perturbed by the loss of macroH2A1.1 and rescued by a KD

Our previous studies in cultured cells suggested that macroH2A1.1 exerts at least part of its impact on metabolism by regulating NAD^+ metabolism (*5*, *15*). Thus, we wondered whether macroH2A1.1 deficiency would also have an impact on NAD^+ metabolism in vivo and whether the phenotypic rescue by a KD would be reflected by normalizations in the NAD^+ axis. For this purpose, we performed targeted metabolomics for NAD^+ and its immediate precursor nicotinamide mononucleotide (NMN) in muscle, liver, and kidney tissue. Although variability of NAD^+ and NMN measurements was high among mice of the same sex and age, patterns emerged when we analyzed NAD^+ and NMN in context of each other (Fig. 6A). In all three tissues, we observed a strong correlation between NAD^+ and NMN levels under WT condition (Fig. 6A). This correlation between both metabolites was lost in macroH2A1.1 KO (Fig. 6A). In murine tissues, NAD^+ can be up to 100-fold more abundant than NMN (*38*). While the amount of NAD^+ and NMN found in the tissues analyzed did not differ between WT and macroH2A1.1 KO mice, we observed a decrease in the hepatic NAD^+/NMN ratio in macroH2A1.1 KO mice (Fig. 6B). KD raised the levels of NAD^+ and NMN in macroH2A1.1-deficient livers and, therefore, normalized the ratio to the one seen in WT tissues (Fig. 6B). For macroH2A1.1-deficient muscle and kidney cells, NAD^+ and NMN levels were unaltered when compared to WT, even under KD (fig. S8, A and B). However, KD restored the correlation between NAD^+ and NMN levels in kidneys from macroH2A1.1 KO mice (Fig. 6C) and increased the correlation in livers (fig. S8C). Together, these results show that loss of macroH2A1.1 perturbs NAD^+ metabolism in a manner that is difficult to interpret. In particular, the correlation between NMN and NAD^+, lost in macroH2A1.1 KO tissues, is a metabolic parameter whose physiological meaning remains to be understood.

In conclusion, histopathologic alterations of the kidney observed in macroH2A1.1 KO mice fed a standard chow diet were associated with deficiencies in water homeostasis, reduced fat metabolization, and a perturbed NAD^+ metabolism. A dietary intervention using KD overcame the metabolic alterations and rescued kidney tissue integrity. Our results suggest that kidney abnormalities are secondary to changes in nutrient metabolization caused by the loss of macroH2A1.1 but not of any other macroH2A isoform.

DISCUSSION

In our study, we provide results from the first systematic and harmonized comparison of isoform-specific KO mice of all macroH2A histone variants at a young age. Only macroH2A1.1 KO mice displayed histopathologic alterations in the kidney as a sex-independent phenotype that was associated with metabolic alterations and rescued through a dietary intervention. Here, we first discuss our results considering the known molecular functions of macroH2A1.1 in compartmental NAD^+ regulation. Second, we reflect on possible explanations of how the observed changes in metabolism, particularly the shift from fat to carbohydrate metabolization, could cause histopathologic alterations in kidneys. Last, we compare our results to previous studies on mice lacking individual or multiple isoforms of macroH2A.

The specificity of the phenotype for macroH2A1.1, but not macroH2A1.2, indicates that it is directly related to its macrodomain, which is the sole difference between both isoforms. While the macrodomain of macroH2A1.1 can bind ADP-ribose moieties, the one of macroH2A1.2 cannot (*10*). In our previous work, we demonstrated that, based on this capacity, macroH2A1.1 has a specific role in regulating the capacity of mitochondria to oxidize fatty acids mediated through cellular NAD^+ metabolism (*5*, *15*). Specifically, we found that, in differentiating muscle cells, macroH2A1.1 is upregulated by a switch in alternative splicing to a level where it acts as an endogenous inhibitor of PARP-1. Because PARP-1 is the most avid consumer of NAD^+ in the nucleus, its activity directly influences the availability of NAD^+ in other organelles such as mitochondria where NAD^+ is essential for the efficient functioning of the respiratory chain, as discussed before (*39*). The depletion of macroH2A1.1 in muscle cells results in increased NAD^+ consumption by PARP-1 in the nucleus, reduced NAD^+ availability in the mitochondria, and, thus, reduced cellular capacity to oxidize fatty acids (*15*). This correlates with the here-described systemic reduction of fat metabolization in macroH2A1.1 KO mice. In both liver and kidney, we further observed alterations in parameters indicating a perturbation of NAD^+ metabolism. This included the loss of linear correlation between NAD^+ and NMN levels. Although apparent, these differences in NAD^+ metabolism are difficult to interpret, and, at present, we cannot draw any conclusion whether changes in NAD^+ are responsible for the systemic metabolic phenotype and the alterations in the kidney or rather a consequence.

Together, loss of macroH2A1.1 leads to metabolic changes in both cultured cells and mice. This is a noncanonical function for a histone variant and particularly remarkable given that macroH2A1.1 constitutes less than 1% of the H2A pool (*7*).

In kidneys from macroH2A1.1 KO mice, we observed histopathologic alterations that included cast formation, a kidney infarct, and the presence of interstitial inflammatory infiltrates. These observations were largely absent in the kidneys of macroH2A1.2 or macroH2A2 KO mice indicating isoform-specificity of the phenotype. The fact that all kidney alterations were rescued by a dietary intervention

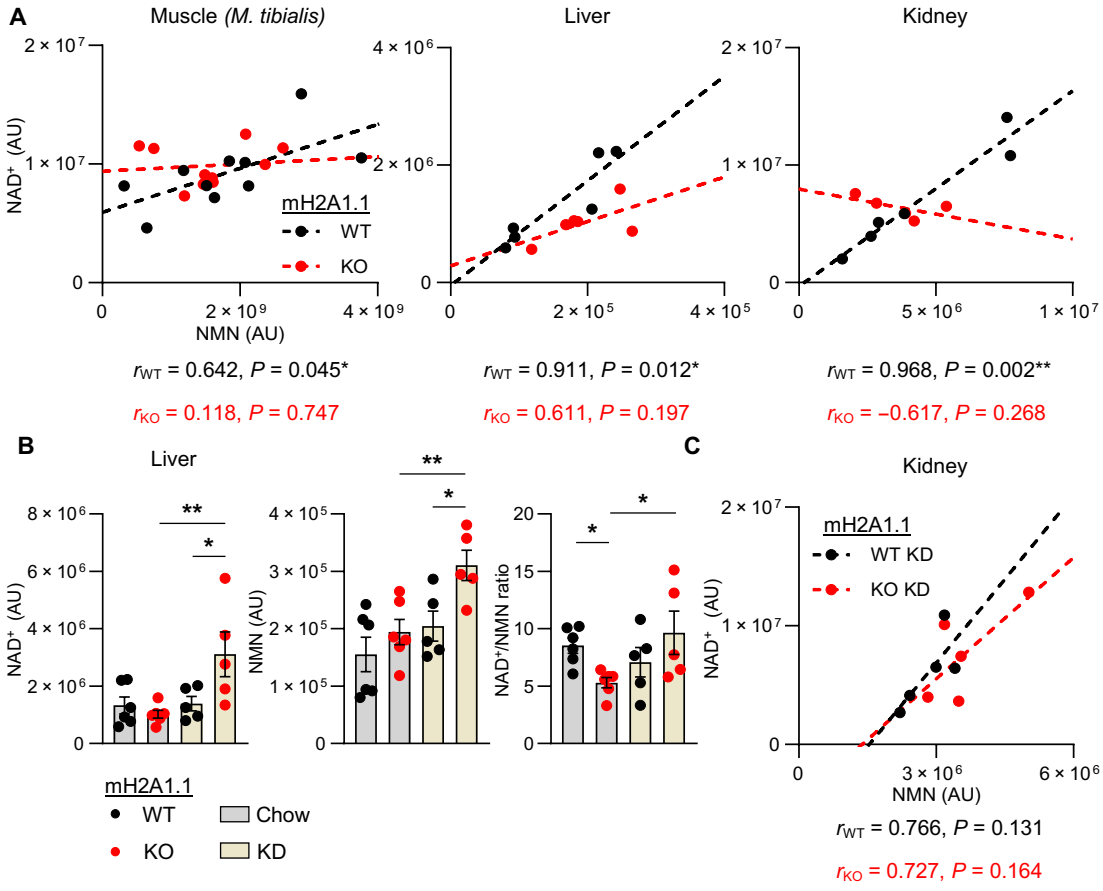

Fig. 6. Tissue-specific impairments of the NAD$^+$ axis arise in macroH2A1.1 KO mice. (**A**) NAD$^+$ and NMN levels were measured by a targeted metabolomics approach in muscle (*Musculus tibialis*), liver, and kidney tissue from male WT or macroH2A1.1 (mH2A1.1) KO mice that received a standard chow diet. Each dot indicates one individual mouse. Correlation of NMN and NAD$^+$ levels was performed, and a linear regression line was inserted. Pearson's correlation coefficient (*r*) is displayed with significance. (**B**) NAD$^+$ and NMN levels were measured by a targeted metabolomics approach in liver tissue from male WT or macroH2A1.1 KO mice that received a standard chow or KD. Data are displayed as means ± SEM. The NAD$^+$ to NMN ratio was calculated. Each dot indicates one individual mouse. Two-way ANOVA with Fisher's LSD (see the Supplementary Materials). (**C**) Correlation of NAD$^+$ and NMN levels in male WT or macroH2A1.1 KO mice after KD is shown. Correlation and linear regression were performed as in (A).

suggests that they are secondary to the metabolic changes caused by macroH2A1.1 depletion. The kidney phenotype could be intrinsic to metabolic changes in the tissue, or a consequence of systemic changes in nutrient metabolization, or a mixture of both. Kidney cells mainly depend on fatty acid oxidation and mitochondrial respiration to cover their high energy demand (*40*). Optimal kidney function and recovery after an insult relies on proper NAD$^+$ homeostasis (*41*, *42*). The kidney is also one of two organs with the highest rates of NAD$^+$ consumption by PARP-1 (*38*), and hyperactivation of PARP-1 contributes to acute and diabetes-induced kidney damage (*43*, *44*). MacroH2A1.1 functions as an endogenous inhibitor of PARP-1, preserves cellular NAD$^+$ pools, and favors optimal respiratory chain function in the mitochondria (*11*, *15*, *45*). Mice with reduced respiratory chain function in filtering kidney cells due to *Pdss1* deletion showed a kidney phenotype that was similar to the phenotype reported here for macroH2A1.1 deletion, albeit more severe (*46*). KD was able to rescue or override the effect of macroH2A1.1 loss on kidney integrity and restored NAD$^+$ metabolism. In this context, it is notable that the oxidation of one molecule of glucose requires four molecules of NAD$^+$, whereas ketone body metabolization requires only one NAD$^+$ molecule (*37*). Some of the beneficial impacts that KDs have in different kidney diseases were attributed to preserving cellular NAD$^+$ levels (*47*, *48*).

Together, NAD$^+$ metabolism and respiratory chain function are intimately linked to kidney health. While we lack mechanistic proof, our present and previously published results (*5*, *15*) support the intriguing hypothesis that perturbations in NAD$^+$ metabolism contribute to the observed macroH2A1.1 loss-of-function phenotype in kidneys. This hypothesis remains to be tested and challenged by future work.

The glycolysis-prone metabolism in macroH2A1.1 KO has the potential to lead to dehydration. Water influx in organisms consists of the direct intake of drinking water or food moisture and the production of metabolic water liberated during the metabolization of nutrients. Metabolic water represents a crucial resource for many animals, especially under conditions of dehydration or fasting (*49*, *50*). Metabolization of 100 g of fat produces about 107 g metabolic water and, thus, substantially more than 100 g of protein or 100 g of carbohydrate that provide 41 g and 60 g, respectively (*51*). Therefore, 1 g of chow diet results in 0.6145 g of metabolic water and 1 g of KD in 0.9739 g of metabolic water when all nutrients are metabolized. Considering the impairment in the fat metabolization of

macroH2A1.1 KO mice, the actual metabolic water generation under chow diet might be even lower. Additional indications for alterations in the water homeostasis of male macroH2A1.1 KO mice under chow diet were increased evaporation, impaired urination, and decreased urinary creatinine levels. Moreover, the appearance of hyaline casts was highly prevalent in kidneys in macroH2A1.1 KO mice but was dramatically reduced under KD. Casts are proteinaceous precipitates caused by high electrolyte concentration and reduced urine flow (*24*, *52*). We found that cast numbers correlated with several indicators of reduced kidney function, including increased serum magnesium, creatinine, and cystatin C levels. Hyaline casts can indicate the beginning of nephropathies and attract immune cells (*25*). Therefore, the appearance of hyaline casts might be functionally connected to the observed inflammatory infiltrates found in macroH2A1.1 KO kidneys. The infiltration of unconventional T cells, such as γδ T cells, was demonstrated for several experimental animal models of kidney diseases (*53*) and correlated with an increase in serum creatinine (*54*). We observed T cell infiltration in male and female macroH2A1.1 KO mice but were only able to find elevated serum creatinine levels in females (fig. S7B). However, sex-specific differences in kidney diseases are commonly observed in humans and mice with males being generally more sensitive (*55*, *56*). We conclude that the observed alterations in the kidney are likely secondary to metabolic changes caused by the loss of macroH2A1.1. Metabolic changes included a systemic reduction in the generation of metabolic water and a reduced capacity to generate energy in tissues caused by alterations in NAD^+ metabolism.

Together, here, we provide the first parallel and harmonized assessment of individual KO mice of all macroH2A isoforms highlighting the sex-independent role of macroH2A1.1 in controlling nutrient metabolization. Specifically, we observed increased glycolysis and reduced fat metabolization in both male and female macroH2A1.1 KO mice that was accompanied by increased glucose tolerance in macroH2A1.1-deficient males. Differences in glucose tolerance were lost upon feeding mice a KD. It is inherently difficult to compare metabolic studies in mice that are highly sensitive to even subtle differences in genetic background, age, diet, and housing conditions. Discrepancies to a previous study (*28*), describing reduced body weight of female macroH2A1.1 KO mice and an unchanged glucose tolerance under standard diet, might be well explained by differences in mouse background (mixed C57BL/6-129S1/Sv), age, and technical setup (prolonged overnight fasting and glucose assessment at different time points of the day). A regular high-fat diet promoted increased glucose tolerance in total macroH2A1 KO and male macroH2A1.1 KO (*19*, *28*), but high-fat diet has a lower fat content than KD (*19*, *28*). In contrast, glucose tolerance was even worse under chow diet in male total macroH2A1 KO mice and unaltered in females (*16*). Others studying a macroH2A1 KO model on a mixed genetic background reported female-specific steatosis with partial penetrance (*17*). Here, the altered expression of hepatic genes involved in lipid homeostasis was demonstrated in accordance with older studies (*16*, *17*). In vitro data also suggest that macroH2A1.1 overexpression reduces lipid droplet size in hepatocytes due to deregulated expression of lipogenic genes (*57*). The transgenic overexpression of macroH2A1.2 in mice led to reduced body weight and improved glucose tolerance (*58*). In our hands, the isoform-specific loss of macroH2A1.2 did not have any major metabolic consequence. In terms of affected genes in the liver, we found similarities at the molecular level between macroH2A1.1 KO mice from our study and mice lacking all three macroH2As (*18*), as both showed an increased expression of hepatic *Fabp5* and *Vldlr* expression. *Vldlr* expression was also significantly up-regulated in a human liver cancer cell line lacking all macroH2A histone variants (*36*). In addition to *Vldlr*, we identified several lipid metabolism–related genes to be up-regulated in livers of macroH2A1.1 KO mice. This included also *Lpin1*, which encodes the transcriptional activator Lipin 1 that forms a complex with PPAR-γ (*59*). The transcription factor PPAR-γ is a key metabolic regulator of the liver, especially in lipid droplet formation (*60*). At present, we cannot distinguish between a direct or indirect role of macroH2A1.1 in the regulation of these genes, but it is plausible that the up-regulation of lipid metabolism genes could be a secondary response to the detected changes in metabolism.

In conclusion, our results demonstrate that a structural chromatin component is able to exert a metabolic function with relevance for organ health. Specifically, the loss of the macrodomain-containing histone variant macroH2A1.1 reduced the systemic nutrient metabolization of fat, which has consequences for kidney integrity. This function is strictly isoform-specific and associated with the previously described capacity of macroH2A1.1 to modulate compartmentalized NAD^+ metabolism in cells (*5*, *15*). A dietary intervention enforcing the metabolization of fat rescued the macroH2A1.1-dependent phenotype in metabolism and the kidney.

MATERIALS AND METHODS

KO generation of macroH2A1

A mouse model to generate isoform-specific KO of macroH2A1 was established by introducing loxP and rox sites into the alternative exon 6 of the encoding gene (*20*). Specifically, macroH2A1.1 heterozygous mice were generated via in vitro fertilization with sperm carrying the floxed exon 6b and WT oocytes. Then, zygotes were treated with 0.3 μM soluble Cre enzyme (catalog #RP-7-S, Excellgen, Rockville, MD, USA) for 30 min to generate heterozygous embryos, which were transferred to previously prepared foster mothers. Genotypic quality control has been carried out by PCR on blastocysts to check Cre-mediated deletion in embryos and ear clip–derived genomic DNA. Exon 6a was excised by mating mice carrying rox sites in the alternative exon 6a with the Dre deleter strain B6.Cg-Pvalbtm3.1(dreo)Hze/J (*61*), generating macroH2A1.2-specific KO mice. WT and homozygous KO mice for macroH2A1.1 and macroH2A1.2 were obtained by mating heterozygous KO mice for macroH2A1.1 and macroH2A1.2, respectively. The mice had been backcrossed for at least 10 generations on a C57BL/6J background.

Genotyping for macroH2A1.1 and macroH2A1.2 was performed with the following primers recognizing the WT allele as well as the tagged allele: H2afy–rox forward: GAACCACCATCTTTCTATTCCAG; H2afy–rox reverse: GCACAGGGCACAGAGGAGAG; H2afy–loxP forward: CTGGGTTGTGAACTGGAGAGG; and H2afy–loxP reverse: AGAAATGTGTGGCTGCTGAG. The PCR program was run with denaturation (1 cycle; 95°C, 5 min), amplification (35 cycles; 95°C, 30 s; 55°C, 30 s; 72°C, 1 min), and termination (1 cycle; 72°C, 10 min).

KO generation of macroH2A2

The macroH2A2 KO mouse model was generated using the IMPC (International Mouse Phenotyping Consortium) targeting strategy with CRISPR-Cas technology (www.mousephenotype.org/understand/the-data/allele-design/) at Helmholtz Zentrum München,

Germany. Guides were designed using the web-based CRISPOR Tool (*62*). A total of four guides were combined to delete exon 3 and 509 base pairs (bp) of flanking intronic sequence including the splice acceptor on the 5′ site and 347 bp including the splice donor on the 3′ site. The single guide RNAs (sgRNAs) were synthesized using the in vitro transcription EnGen kit (catalog #E3322S, New England Biolabs, MA, USA). DNA oligonucleotides for sgRNA synthesis were generated with the NEB tool (https://sgrna.neb.com/#!/sgrna) and ordered from metabion (Planegg, Germany). Following in vitro transcription, RNA was purified using the RNA Clean & Concentrator Kit (catalog #R1017, Zymo, Irvine, CA, USA). The deletion allele injection mixes consisted of Cas9 protein (200 ng/μl; catalog #1081059, IDT, Coralville, IA, USA) and sgRNAs (50 ng/μl) in a final volume of 5 μl of Opti-MEM (catalog #11058021, Thermo Fisher Scientific).

The sgRNA/Cas9 mixture was electroporated into the pronuclear stage of C57BL/6NCrl zygotes. For a single electroporation event, 50 one-cell stage embryos were filled into a 1-mm glass chamber of a NEPA21 electroporator (NEPA GENE Co. Ltd., Ichikawa City, Japan), filled with 5 μl of Opti-MEM containing sgRNA-ribonucleoprotein complexes following a standardized electroporation protocol. Injected zygotes were cultured overnight, developed into two-cell embryos, and were transferred into pseudo-pregnant (day 0.5 postcoitum) CD-1 females on the day after the injection. On average, 16 embryos were used per recipient female.

The guide sequences were as follows: (1) GCGATCACTCTATGATCGCC TGG; (2) GCTGCGGGGGTAAATGGTAT GGG; (3) ATTTGTAGCACACATCCGAC AGG; and (4) AAGAAGGTTGCTCCGTCCCT TGG. For genotype analysis, genomic DNA was extracted from tissue samples collected from mice during ear labeling at weaning age (3 weeks old), and PCR reaction was performed with the following *Macroh2a2*-specific primers, ordered from Metabion: Macroh2a2_F: ACCCACACTTTATCCTCCACC; Macroh2a2_R: TGTATTGGTCACTGTGGCATG; and Macroh2a2_wtR2: CTTCCTAGGCACAGTAGGCTG.

The PCR program using HotStarTaq DNA polymerase (catalog #203203, QIAGEN, Germantown, MD, USA) was run with denaturation (1 cycle; 94°C, 5 min), amplification (10 cycles; 94°C, 30 s; touchdown from 65°C to 55°C, 30 s; 72°C, 45 s), amplification (25 cycles; 94°C, 30 s; 55°C, 30 s; 72°C, 45 s), and termination (1 cycle; 72°C, 10 min). The mutation was verified by Sanger sequencing. The mutation is predicted to cause a change of amino acid sequence after residue 58 and early truncation 52 amino acids later.

Generation of mH2A1.2/mH2A2 DKO mice

To generate mH2A1.2/mH2A2 DKO ("macroH2A1.1 only") mice, we crossed C57BL/6 macroH2A1.2 KO mice (*63*) to 129S1/Sv macroH2A2 KO mice (*18*), provided by E. Bernstein. Heterozygous macroH2A1.2/+; macroH2A2/+ mice were intercrossed to generate DKOs for macroH2A1.2 and macroH2A2 isoforms. Offspring with WT alleles was used as controls.

Mouse housing

Animal housing was performed in strict accordance with directive 2010/63/EU and the local and federal government. All mice were housed in individually ventilated caging (IVC) systems (Sealsafe plus, GM500, Tecniplast, Buguggiate, Italy) under specific pathogen-free conditions with a maximum cage density of five adult mice per cage. IVC systems operate with positive pressure. All mice received autoclaved wood chips (LIGNOCEL Select Fine, J. Rettenmaier & Soehne GmbH, Rosenberg, Germany) and paper stripes (ARBOCEL crinclets natural, J. Rettenmaier & Soehne GmbH) as bedding and nesting material, irradiated standard diet (catalog #1314) or KD (catalog #C1084) for rodents (Altromin Spezialfutter GmbH, Lage, Germany), and sterile-filtered tap water ad libitum. The light was adjusted to a 12-hour/12-hour light/dark cycle with a 10-min period of dimmed light to simulate sunrise/sunset; temperature and relative humidity are regulated to 22 ± 2°C and 55 ± 10%, respectively. Health monitoring was based on quarterly exhaust air dust PCR analysis for all FELASA (Federation of European Laboratory Animal Science Associations)–listed agents. Autonomic functions including urination and defecation were tested during a modified SHIRPA protocol with a test duration of ~3 min (*64*).

Mouse phenotyping pipeline

At the German Mouse Clinic (GMC), female and male mouse cohorts of KOs and corresponding WT controls were subjected to an extensive phenotypic screening (*65*, *66*). Cohort of 15 male and 14 female macroH2A1.1 were compared to 15 male and 13 female controls, and 10 male and 9 female macroH2A1.2 were compared to 11 male and 5 female controls. In addition, 15 male and female macroH2A1.1 and 15 male and female controls fed a KD were analyzed. Furthermore, cohorts of 9 male and 10 female macroH2A2 were compared with 10 control males and 13 control females. The selected sample size is based on long-term experience and is sufficient to find a medium difference of one standard deviation with a power of 0.8 and alpha of 0.05. The phenotyping measurements were taken from weeks 8 to 16 for macroH2A2, and weeks 9 to 19 for macroH2A1.1 and macroH2A1.2. mouse lines. The assignment of experimental groups was based on the genotype of the animals, and metadata for each data point were recorded throughout the measurements. Randomization for sample taking and automatic measurements was performed. The phenotypic tests were part of the GMC screening pipeline and performed according to standardized protocols as described before (*67*–*69*). When suitable, the experimenter was blinded. We strongly adhere to the ARRIVE (Animal Research: Reporting of In Vivo Experiments) guidelines, and detailed information regarding sample size determination, inclusion/exclusion criteria, randomization, and blinding can be found online (www.mouseclinic.de/about-gmc/the-arrive-essential-10/index.html). All animal experiments at the GMC were approved by the responsible ethics committee from the authority of the district government of Upper Bavaria, Germany under license numbers 16-46 and 15-068. Animal numbers may vary depending on the test performed, as indicated in the respective figure or table.

Metabolic screen

The primary metabolic screen focused on the determination of energy expenditure by indirect calorimetry (*70*). Body mass, food intake, and locomotor activity were monitored under ad libitum conditions. High-precision CO_2 and O_2 sensors measured the difference in CO_2 and O_2 concentrations in air flowing through control and animal cages. Based on this, the rates of oxygen consumption and CO_2 production were calculated with the following formulas (*71*): net glucose oxidation: c [g/min] = 4.55 V_{CO2} − 3.21 V_{O2}; net lipid oxidation: f [g/min] = 1.67 V_{O2} − 1.67 V_{CO2}. These calculations do not consider nitrogen metabolism and are only valid for standard conditions. The RER expresses the ratio of the volume CO_2/volume

O_2. Heat production (HP) was calculated from the volume of O_2 and RER using the formula: HP [mW] = (4.44 + 1.43 RER) · V_{O2} [ml · h^{-1}]. The metabolic screen was performed at room temperature (23°C) under standard housing conditions. Each mouse was placed individually in a chamber for a period of 21 hours (from 13:00 to 10:00 CET). Food intake was monitored by continuously weighing food hoppers that were attached to electronic scales. Infrared light beam frames set up around the cages measured physical activity. This system allows the measurement of distance traveled per time interval.

Body composition

The body composition, in particular lean and fat mass, was determined with either time domain nuclear magnetic resonance using a Bruker minispec LF50 analyzer (Bruker Corp., Billerica, MA, USA) or a dual-energy x-ray absorptiometry (DEXA) scan using a Faxitron Ultrafocus equipped with 10 cm–by–15 cm complementary metal-oxide semiconductor detector (Faxitron Bioptics, LLC, Tucson, AZ, USA). Image acquisition for DEXA and analysis was performed using VisionDXA software (Faxitron Bioptics, LLC). Mice were anesthetized before the procedures and body weights were recorded.

Intraperitoneal glucose tolerance test

Mice were used for the glucose tolerance test after a 6-hour food withdrawal. For the determination of the fasting blood glucose level, the tip of the tail was scored using a sterilized scalpel blade, and a small drop of blood was analyzed with an Accu-Chek Aviva glucose analyzer (Roche, Mannheim, Germany). Thereafter, mice were injected intraperitoneally with 2 g of glucose/kg of body weight using a 20% glucose solution. Fifteen, 30, 60, and 120 min after glucose injection, additional blood samples (one drop each) were collected and used to determine blood glucose levels as described before. Repeated bleeding was induced by removing the clot from the first incision and gently massaging the tail of the mouse.

Clinical chemistry

Heparinized blood was collected from mice and left at room temperature for 1 to 2 hours. Afterward, cells and plasma were separated by a centrifugation step (10 min, 4600 rpm, 4°C; Hettich ROTANTA 460c). Plasma aliquots were transferred into reaction tubes and used without (plasma of unfed mice) or with prior dilution 1:2 with deionized water (ad libitum fed mice). Samples were mixed for a few seconds (Vortex-Genie, Scientific Industries, NY, USA) to prevent clotting and then centrifuged again for 10 min at 5000*g* and 8°C (Biofuge fresco, Heraeus, Hanau, Germany) before analysis. The clinical chemistry screen was performed using a Beckman Coulter AU480 autoanalyzer and adapted reagents from Beckman Coulter (Krefeld, Germany), including the following enzymes and substrates: ALAT/GPT (EC 2.6.1.2), albumin, AP (EC 3.1.3.1), ASAT/GOT (EC 2.6.1.1), cholesterol and HDL cholesterol, glucose, lactate, magnesium, sodium, total protein, and urea. In addition, the AU480 analyzer was used with Beckman Coulter test kits (Urine/CSF Albumin catalog #B38858 and Enzymatic Creatinine catalog #OSR61204) with calibrators from Beckman Coulter (Urine Calibrator catalog #B64606 and Urine Albumin Calibrator catalog #B38859) and controls from Bio-Rad (Liquicheck Level 1 and 2, Bilevel MiniPak 198X). Spontaneous urine samples were collected for 2 days from the aged cohort of age- and sex-matched WT, macroH2A1.1, and macroH2A1.2 KO mice and stored at −80°C until analysis. Plasma insulin and leptin levels were determined using an enzyme-linked immunosorbent assay (ELISA; mouse/rat insulin kit catalog #K152BZC and mouse metabolic kit catalog #K15124C, Meso Scale Discovery, Rockville, MD, USA) and a MESO QuickPlex SQ 120 sector imager (Meso Scale Discovery). For hematological analysis, blood-EDTA samples were analyzed on a Sysmex XT-2000iV blood cell counter (Sysmex, Norderstedt, Germany). Cystatin C levels were measured using the commercial ELISA kit Abcam catalog #ab11959 (Mouse Cystatin C ELISA Kit), following the manufacturer's protocol. The assay has a detection range of 312 to 20,000 pg/ml and a sensitivity of <10 pg/ml. Optical density was read at 450 nm, 30 min after the addition of the stop solution.

Macroscopic and histological analyses

Mice were sacrificed by CO_2 inhalation, and all organs were weighed. Afterward, organs were fixed in 4% buffered formalin and embedded in paraffin for histological examination. Sections (2-µm thick) from all isolated organs were cut and stained with H&E. A Leica BOND RX (Leica Biosystems) automatic stainer was used for immunohistochemistry. Heat-induced antigen retrieval was performed with citrate buffer (pH 6) for 30 min (catalog #AR9961, BOND Epitope Retrieval Solution, Leica Biosystems). Antibodies against CD3 (Clone SP7, catalog #ZYT-RBG024, Zytomed Systems; RRID:AB_2864584) were used, and the staining was detected with DAB chromogen. Periodic acid–Schiff staining was performed to characterize the renal casts. The slides were digitally scanned in a NanoZoomer 2.0 HT device (Hamamatsu, Japan). Pictures were acquired using NDP.view2 software.

Transepidermal water loss

TEWL is defined as the measurement of the quantity of water that passes from inside a body through the epidermal layer (skin) to the surrounding atmosphere via diffusion and evaporation processes. Mouse skin was analyzed in a noninvasive manner with a special Tewameter (AquaFlux AF200, Biox Systems Ltd., UK) that was placed on the skin. During a short time of 60 to 90 s, TEWL [g/(m^2h)] was recorded.

RNA isolation and cDNA synthesis

For KO quality control, RNA was isolated from brain tissue using the RNeasy Mini Kit (catalog #74104, QIAGEN) according to the manufacturer's instructions. cDNA was obtained using the ProtoScript II Reverse Transcriptase (catalog # M0368, New England Biolabs Inc., Ipswich, MA, USA). A 1:5 dilution of the cDNA was used for PCR with the Macroh2a2_exon_2 primers to detect the deletion of exon 3. The mutation was verified by Sanger sequencing. For analysis of liver and kidney, RNA was isolated from at least 20 mg of homogenized tissue using an automatic purification platform (Maxwell RSC Instrument, Promega, Madison, WI, USA) and the corresponding Maxwell RSC simplyRNA Tissue Kit (Promega) according to the manufacturer's recommendations. cDNA was synthesized using the first strand cDNA synthesis kit (Thermo Fisher Scientific) combining random hexamer and oligo(dT) primers.

RT-qPCR

RT-qPCR was performed using LightCycler 480 SYBR Green I Master (Roche) and target-specific primers, ordered from IDT, listed below according to the manufacturer's recommendations. Reactions were performed in triplicates for the target and the housekeeping genes (*Gapdh* and *Rplp0*) using a QuantStudio 7 Flex Real-Time PCR System (Thermo Fisher Scientific). Fold inductions were calculated based on the ΔΔCT method and normalized to the mean of

the control (WT under chow diet). The primers used were as follows: *Angptl8*: GTCGGAGATTCAGGTGGAAGA, GTAGTCTCCGTACAGTGTCCC; *Arl4a*: ACAAGACCTGAGGAACTCGC, CGAGTCCTTCCTTTAGCCCA; *Camk2b*: GCACGTCATTGGCGAGGAT, ACGGGTCTCTTCGGACTGG; *Camkk2*: CCTGGACATGAATGGACGCT, GCACGCAGTCCTGCAAAC; *Cst3*: TCGCTGTGAGCGAGTACAAC, CCAGCCACGAGCTGCTTAC; *Fabp5*: TCCCACCATGGCCAGTCTTA, AAGAGCCAGTCCTACTCCTAGC; *Gapdh*: TGCACCACCAACTGCTTAG, GATGCAGGGATGATGTTC; *Habp4*: CCCTGGGGATCAGGTAAAGAC, CTCCAACTCAGGAACTTTGGCT; *Lpin1*: CTCCGCTCCCGAGAGAAAG, TCATGTGCAAATCCACGGACT; *Lpin2*: GAAGTGGCGGCTCTCTATTTC, AGAGGGTTACATCAGGCAAGT; mH2A1.1: CCTACAGACGGCTTCACTGTC, GTGTAGAAGTCAGTGTTTGTCG; mH2A1.2: CCTACAGACGGCTTCACTGTC, GGTCAATGTCAGCATTGGTAGG; *MacroH2A2*: GCTGGAAGAGACCATCAAAAA, CGAAGTGAGCCGAGATGG; Macroh2a2_exon_2: ATTGTGTAGGTGCCAAGAGACCA, TCTTGGACGTCCGTGGCTTGGTG; *Noct*: CGTCCCCGAACAGTGAGTT, AGAACAGCCCTGCATTCCTC; *Per1*: CGGAGCTTCTGGGTTGCG, TAATCACGACACCTGGCCGT; *Plcd3*: CCGACTCCGACCAAGACAGTA, AGACGCTCGTTGTTGGAATGG; *Rplp0*: ACATCTCCCCCTTCTCCTTC, TACCCGATCTGCAGACACAC; *Sfi1*: TTGGGGAGCAGCAGTTAGAGA, CGGACCAGGAACATTCGGC; *Slc35d2*: CTGGCTCTGACCTCACATTCA, AGCTCCTTCGGGTCCATTTTC; *Unc5a*: TTGTCAAGAACAAGCCCGTG, CATGGTTGGCAATCCGCTG; and *Vldlr*: AAGGCCATCTTCAGTGCCTC, GAAGCCGCATCAGTCCAGTA.

Transcriptomic analysis

Total RNA (2 μg) was submitted to Novogene (Cambridge, UK) for the preparation of RNA-seq libraries with a poly(A) selection and sequencing in an Illumina NovaSeq 6000 using 150-bp paired-end reads obtaining >30 million reads per sample. Sequencing reads were trimmed for adapter sequence removal using Trim Galore! (www.bioinformatics.babraham.ac.uk/projects/trim_galore/), aligned with STAR (*72*) to mouse genome annotation GRCm38 (Genome Reference Consortium Mouse Reference 38) and quantified with FeatureCounts (*73*) to produce a count table at the gene level. Differential gene expression analysis was performed with the R package DESeq2 (*74*). The experimental groups for the model design formula were defined as a combination of tissue and genotype, and contrasts between different genotypes for each tissue were obtained. DEGs were determined with an adjusted *P* value cutoff of 0.05. For principal components analysis and heatmap visualizations, the variance-stabilized log 2 transformation of the count data was used. Volcano plots were generated using ggplot2 (https://doi.org/10.1007/978-3-319-24277-4). Heatmaps were generated using pheatmap (https://CRAN.R-project.org/package=pheatmap). GO term grouping was performed using the REVIGO tool (*75*) with the following settings: large clusters 0.9, Resnik algorithm, *Mus musculus*.

Western blot

Protein extraction was performed by resuspending homogenized tissue in radioimmunoprecipitation assay lysis buffer and incubation for 10 min on ice. Lysates were sonicated for 5 min with an ultrasonic processor (UP50H, Hielscher Ultrasonics GmbH, Germany), centrifuged for 10 min at 13,000*g*, 4°C, and the supernatant was transferred. Protein concentrations were measured using a bicinchoninic acid (BCA) kit (Pierce BCA Protein Assay Kit, catalog #23225, Thermo Fisher Scientific) and mixed with Laemmli buffer. After heating at 95°C for 10 min, 50 μg of sample was loaded per lane on 14% polyacrylamide gels and run at 70 to 100 V for 60 min to achieve optimal separation and then transferred at 300 mA for 90 min onto a nitrocellulose membrane (Amersham Protran, 0.45 μm, catalog #10600002, Cytiva). After the transfer, the membranes were blocked using 5% nonfat milk (Nestlé) in tris-buffered saline with Tween 20 (TBS-T) for 60 min. Membranes were incubated with primary antibodies overnight at 4°C. The day after, membranes were washed thrice with TBS-T for 10 min and incubated for 1 hour at room temperature with fluorophore-conjugated secondary anti-rabbit antibodies (LI-COR Biosciences IRDye 680RD or IRDye 800CW). Membranes were then washed again thrice with TBS-T for 10 min. For the detection of fluorescent signals, the dried membranes were scanned with an Odyssey CLx Imager. The following polyclonal rabbit antibodies were used for this study: anti-H3 (catalog #ab1791, Abcam; RRID:AB_302613), anti-macroH2A1.1 (*76*), anti-macroH2A1.2 (catalog #4827S, Cell Signaling Technology, Inc.; RRID:AB_1950388), and anti-macroh2A2 (*77*, *78*). All antibodies used for Western blot were validated either by the distributor or in the respective research study in the case of non-commercial antibodies. Size of the detected proteins was as expected compared to Chameleon Duo Pre-stained Protein Ladder (LI-COR Biotechnology, Lincoln, NE, USA).

Metabolomics

Metabolites from kidneys and livers were extracted into solvent by adding 250 μl of cold acetonitrile:methanol:water (5:4:1/v:v:v). Samples were vortexed previously to three cycles of incubation in liquid nitrogen for 30 s, sonicated for 30 s in a water bath, and vortexed for 30 s. Samples were kept for 1 hour to enable protein precipitation in the freezer. Subsequently, samples were centrifuged for 10 min at 4°C and 12,000 rpm, and the supernatant was transferred to a liquid chromatography–mass spectrometry (LC-MS) vial. LC-MS was performed with a Vanquish Horizon UHPLC System (Thermo Fisher Scientific, Waltham, MA, USA) interfaced with an Orbitrap ID-X Tribrid Mass Spectrometer (Thermo Fisher Scientific). Metabolites were separated with an ACQUITY BEH HILIC 2.1 mm by 150 mm, 1.7-μm column (Waters Corp., MS, USA). The mobile phase A was 50 mM ammonium acetate in water, and mobile phase B was acetonitrile. Separation was conducted under the following gradient: 0 to 1 min, isocratic 90% B; 1 to 3 min decreased to 50% B; 3 to 4 min, isocratic 50% B, 4 to 4.5 min, increased to 90% B; and 4.5 to 7.5 min, re-equilibration column 90% B. The flow was 0.6 ml/min. The injection volume was 5 μl. Samples were analyzed in targeted selected ion monitoring mode in positive mode. The used parameters for MS were isolation window (mass/charge ratio), 2; spray voltage, 4000 V; sheath gas, 50; auxiliary gas, 10; ion transfer tube temperature, 300°C; vaporizer temperature, 300°C; Orbitrap resolution, 60,000; radio frequency lens (%), 60; automatic gain control target, 2×10^5; and maximum injection time, 200 ms.

Statistical analysis

GraphPad Prism software, version 8, was used for data processing and statistical analysis. Raw data values can be found in table S6. Statistical tests are indicated in the corresponding figure legends. Data in bars are displayed as means ± SEM. Boxes display Q1 and Q3, the median as a band, and minimum to maximum range. In each legend, *n* indicates the number of biological replicates. The used statistical test is given in the figure legend. Two-sided tests

were performed with the testing level alpha set at 0.05. In the figures, stars are used to flag the levels of significance for three of the commonly used levels. If a *P* value is less than 0.05, it is flagged with one star (*). If a *P* value is less than 0.01, it is flagged with two stars (**). If a *P* value is less than 0.001, it is flagged with three stars (***). A *P* value less than 0.05 was considered statistically significant. Linear mixed-effect models were fitted in R with the package lme4, and a likelihood ratio test was performed between full and reduced models to evaluate the significance of the genotype factor. Model formulas, parameter estimates, and likelihood ratio test results are available in the Supplementary Materials.

Supplementary Materials

The PDF file includes:

Figs. S1 to S8
Tables S1, S3, and S4
Extended Data E1
Legends for tables S2, S5, and S6

Other Supplementary Material for this manuscript includes the following:

Tables S2, S5, and S6

REFERENCES AND NOTES

1. T. Misteli, The self-organizing genome: Principles of genome architecture and function. *Cell* **183**, 28–45 (2020).
2. K. Zhou, G. Gaullier, K. Luger, Nucleosome structure and dynamics are coming of age. *Nat. Struct. Mol. Biol.* **26**, 3–13 (2019).
3. J. G. M. Rack, D. Perina, I. Ahel, Macrodomains: Structure, function, evolution, and catalytic activities. *Annu. Rev. Biochem.* **85**, 431–454 (2016).
4. C. Rivera-Casas, R. Gonzalez-Romero, M. S. Cheema, J. Ausió, J. M. Eirín-López, The characterization of macroH2A beyond vertebrates supports an ancestral origin and conserved role for histone variants in chromatin. *Epigenetics* **11**, 415–425 (2016).
5. I. Guberovic, S. Hurtado-Bagès, C. Rivera-Casas, G. Knobloch, R. Malinverni, V. Valero, M. M. Leger, J. García, J. Basquin, M. Gómez de Cedrón, M. Frigolé-Vivas, M. S. Cheema, A. Pérez, J. Ausió, A. Ramírez de Molina, X. Salvatella, I. Ruiz-Trillo, J. M. Eirin-Lopez, A. G. Ladurner, M. Buschbeck, Evolution of a histone variant involved in compartmental regulation of NAD metabolism. *Nat. Struct. Mol. Biol.* **28**, 1009–1019 (2021).
6. I. Guberovic, M. Farkas, D. Corujo, M. Buschbeck, Evolution, structure and function of divergent macroH2A1 splice isoforms. *Semin. Cell Dev. Biol.* **135**, 43–49 (2023).
7. M. Buschbeck, S. B. Hake, Variants of core histones and their roles in cell fate decisions, development and cancer. *Nat. Rev. Mol. Cell Biol.* **18**, 299–314 (2017).
8. G. Leroy, P. A. Dimaggio, E. Y. Chan, B. M. Zee, M. A. Blanco, B. Bryant, I. Z. Flaniken, S. Liu, Y. Kang, P. Trojer, B. A. Garcia, A quantitative atlas of histone modification signatures from human cancer cells. *Epigenetics Chromatin* **6**, 20 (2013).
9. S. Chakravarthy, S. K. Y. Gundimella, C. Caron, P.-Y. Perche, J. R. Pehrson, S. Khochbin, K. Luger, Structural characterization of the histone variant macroH2A. *Mol. Cell. Biol.* **25**, 7616–7624 (2005).
10. G. Kustatscher, M. Hothorn, C. Pugieux, K. Scheffzek, A. G. Ladurner, Splicing regulates NAD metabolite binding to histone macroH2A. *Nat. Struct. Mol. Biol.* **12**, 624–625 (2005).
11. M. Kozlowski, D. Corujo, M. Hothorn, I. Guberovic, I. K. Mandemaker, C. Blessing, J. Sporn, A. Gutierrez-Triana, R. Smith, T. Portmann, M. Treier, K. Scheffzek, S. Huet, G. Timinszky, M. Buschbeck, A. G. Ladurner, MacroH2A histone variants limit chromatin plasticity through two distinct mechanisms. *EMBO Rep.* **19**, e44445 (2018).
12. N. G. Simonet, J. K. Thackray, B. N. Vazquez, A. Ianni, M. Espinosa-Alcantud, J. Morales-Sanfrutos, S. Hurtado-Bagès, E. Sabidó, M. Buschbeck, J. Tischfield, C. de la Torre, M. Esteller, T. Braun, M. Olivella, L. Serrano, A. Vaquero, SirT7 auto-ADP-ribosylation regulates glucose starvation response through mH2A1. *Sci. Adv.* **6**, eaaz2590 (2020).
13. M. J. Gamble, K. M. Frizzell, C. Yang, R. Krishnakumar, W. L. Kraus, The histone variant macroH2A1 marks repressed autosomal chromatin, but protects a subset of its target genes from silencing. *Genes Dev.* **24**, 21–32 (2010).
14. H. Chen, P. D. Ruiz, L. Novikov, A. D. Casill, J. W. Park, M. J. Gamble, MacroH2A1.1 and PARP-1 cooperate to regulate transcription by promoting CBP-mediated H2B acetylation. *Nat. Struct. Mol. Biol.* **21**, 981–989 (2014).
15. M. Posavec Marjanović, S. Hurtado-Bagès, M. Lassi, V. Valero, R. Malinverni, H. Delage, M. Navarro, D. Corujo, I. Guberovic, J. Douet, P. Gama-Perez, P. M. Garcia-Roves, I. Ahel, A. G. Ladurner, O. Yanes, P. Bouvet, M. Suelves, R. Teperino, J. A. Pospisilik, M. Buschbeck, MacroH2A1.1 regulates mitochondrial respiration by limiting nuclear NAD+ consumption. *Nat. Struct. Mol. Biol.* **24**, 902–910 (2017).
16. L. N. Changolkar, C. Costanzi, N. A. Leu, D. Chen, K. J. McLaughlin, J. R. Pehrson, Developmental changes in histone macroH2A1-mediated gene regulation. *Mol. Cell. Biol.* **27**, 2758–2764 (2007).
17. M. Boulard, S. Storck, R. Cong, R. Pinto, H. Delage, P. Bouvet, Histone variant macroH2A1 deletion in mice causes female-specific steatosis. *Epigenetics Chromatin* **3**, 8 (2010).
18. J. R. Pehrson, L. N. Changolkar, C. Costanzi, N. A. Leu, Mice without MacroH2A histone variants. *Mol. Cell. Biol.* **34**, 4523–4533 (2014).
19. F. Sheedfar, M. Vermeer, V. Pazienza, J. Villarroya, F. Rappa, F. Cappello, G. Mazzoccoli, F. Villarroya, H. Van Der Molen, M. H. Hofker, D. P. Koonen, M. Vinciguerra, Genetic ablation of macrohistone H2A1 leads to increased leanness, glucose tolerance and energy expenditure in mice fed a high-fat diet. *Int. J. Obes.* **39**, 331–338 (2015).
20. O. Bereshchenko, O. Lo Re, F. Nikulenkov, S. Flamini, J. Kotaskova, T. Mazza, M. M. Le Pannérer, M. Buschbeck, C. Giallongo, G. Palumbo, G. Li Volti, V. Pazienza, L. Cervinek, C. Riccardi, L. Krejci, S. Pospisilova, A. F. Stewart, M. Vinciguerra, Deficiency and haploinsufficiency of histone macroH2A1.1 in mice recapitulate hematopoietic defects of human myelodysplastic syndrome. *Clin. Epigenetics* **11**, 121 (2019).
21. V. Chiodi, M. R. Domenici, T. Biagini, R. De Simone, A. M. Tartaglione, M. Di Rosa, O. Lo Re, T. Mazza, V. Micale, M. Vinciguerra, Systemic depletion of histone macroH2A1.1 boosts hippocampal synaptic plasticity and social behavior in mice. *FASEB J.* **35**, e21793 (2021).
22. F. Heller, M. T. Lindenmeyer, C. D. Cohen, U. Brandt, D. Draganovici, M. Fischereder, M. Kretzler, H. J. Anders, T. Sitter, I. Mosberger, D. Kerjaschki, H. Regele, D. Schlöndorff, S. Segerer, The contribution of B cells to renal interstitial inflammation. *Am. J. Pathol.* **170**, 457–468 (2007).
23. Q. Wei, Z. Dong, Mouse model of ischemic acute kidney injury: Technical notes and tricks. *Am. J. Physiol. Renal Physiol.* **303**, F1487–F1494 (2012).
24. Z. Dvanajscak, L. N. Cossey, C. P. Larsen, A practical approach to the pathology of renal intratubular casts. *Semin. Diagn. Pathol.* **37**, 127–134 (2020).
25. T.-H. Wu, K.-J. Li, C.-L. Yu, C.-Y. Tsai, Tamm–Horsfall protein is a potent immunomodulatory molecule and a disease biomarker in the urinary system. *Molecules* **23**, 200 (2018).
26. K. Teramoto, Y. Tsurekawa, M. A. Suico, S. Kaseda, K. Omachi, T. Yokota, M. Kamura, M. Piruzyan, T. Kondo, T. Shuto, E. Araki, H. Kai, Mild electrical stimulation with heat shock attenuates renal pathology in adriamycin-induced nephrotic syndrome mouse model. *Sci. Rep.* **10**, 18719 (2020).
27. C. P. Peter, J. D. Burek, M. J. Van Zwieten, Spontaneous nephropathies in rats. *Toxicol. Pathol.* **14**, 91–100 (1986).
28. V. Chiodi, F. Rappa, O. Lo Re, G. N. Chaldakov, B. Lelouvier, V. Micale, M. R. Domenici, M. Vinciguerra, Deficiency of histone variant macroH2A1.1 is associated with sexually dimorphic obesity in mice. *Sci. Rep.* **13**, 19123 (2023).
29. N. D. Palmer, M. C. Y. Ng, P. J. Hicks, P. Mudgal, C. D. Langefeld, B. I. Freedman, D. W. Bowden, Evaluation of candidate nephropathy susceptibility genes in a genome-wide association study of African American diabetic kidney disease. *PLOS ONE* **9**, e88273 (2014).
30. W. Wang, W. B. Reeves, G. Ramesh, Netrin-1 and kidney injury. I. Netrin-1 protects against ischemia-reperfusion injury of the kidney. *Am. J. Physiol. Renal Physiol.* **294**, 739–747 (2008).
31. M. A. Maranduca, C. T. Cozma, A. Clim, A. C. Pinzariu, I. Tudorancea, I. P. Popa, C. I. Lazar, R. Moscalu, N. Filip, M. Moscalu, M. Constantin, D. V. Scripcariu, D. N. Serban, I. L. Serban, The molecular mechanisms underlying the systemic effects mediated by parathormone in the context of chronic kidney disease. *Curr. Issues Mol. Biol.* **46**, 3877–3905 (2024).
32. S. Kishi, T. Nakashima, T. Goto, H. Nagasu, C. R. Brooks, H. Okada, K. Tamura, T. Nakano, I. Narita, S. Maruyama, Y. Yano, T. Yokoo, T. Wada, J. Wada, M. Nangaku, N. Kashihara, Association of serum magnesium levels with renal prognosis in patients with chronic kidney disease. *Clin. Exp. Nephrol.* **28**, 784–792 (2024).
33. L. R. Van Nynatten, M. R. Miller, M. A. Patel, M. Daley, G. Filler, S. Badrnya, M. Miholits, B. Webb, C. W. McIntyre, D. D. Fraser, A novel multiplex biomarker panel for profiling human acute and chronic kidney disease. *Sci. Rep.* **13**, 21210 (2023).
34. K. Soto, S. Coelho, B. Rodrigues, H. Martins, F. Frade, S. Lopes, L. Cunha, A. L. Papoila, P. Devarajan, Cystatin C as a marker of acute kidney injury in the emergency department. *Clin. J. Am. Soc. Nephrol.* **5**, 1745–1754 (2010).
35. Z. Tian, M. Liang, Renal metabolism and hypertension. *Nat. Commun.* **12**, 963 (2021).
36. D. Corujo, R. Malinverni, J. Carrillo-Reixach, O. Meers, A. Garcia-Jaraquemada, M. M. Le Pannérer, V. Valero, A. Pérez, Á. Del Río-Álvarez, L. Royo, B. Pérez-González, H. Raurell, R. D. Acemel, J. M. Santos-Pereira, M. Garrido-Pontnou, J. L. Gómez-Skarmeta, L. Pasquali, J. Manyé, C. Armengol, M. Buschbeck, MacroH2As regulate enhancer-promoter contacts affecting enhancer activity and sensitivity to inflammatory cytokines. *Cell Rep.* **39**, 110988 (2022).
37. M. Elamin, D. N. Ruskin, P. Sacchetti, S. A. Masino, A unifying mechanism of ketogenic diet action: The multiple roles of nicotinamide adenine dinucleotide. *Epilepsy Res.* **167**, 106469 (2020).

38. V. Mori, A. Amici, F. Mazzola, M. Di Stefano, L. Conforti, G. Magni, S. Ruggieri, N. Raffaelli, G. Orsomando, Metabolic profiling of alternative NAD biosynthetic routes in mouse tissues. *PLOS ONE* **9**, e113939 (2014).
39. S. Hurtado-Bagès, I. Guberovic, M. Buschbeck, The MacroH2A1.1 – PARP1 axis at the intersection between stress response and metabolism. *Front. Genet.* **9**, 417 (2018).
40. H. M. Kang, S. H. Ahn, P. Choi, Y. A. Ko, S. H. Han, F. Chinga, A. S. D. Park, J. Tao, K. Sharma, J. Pullman, E. P. Bottinger, I. J. Goldberg, K. Susztak, Defective fatty acid oxidation in renal tubular epithelial cells has a key role in kidney fibrosis development. *Nat. Med.* **21**, 37–46 (2015).
41. K. M. Ralto, E. P. Rhee, S. M. Parikh, NAD^+ homeostasis in renal health and disease. *Nat. Rev. Nephrol.* **16**, 99–111 (2020).
42. M. T. Tran, Z. K. Zsengeller, A. H. Berg, E. V. Khankin, M. K. Bhasin, W. Kim, C. B. Clish, I. E. Stillman, S. A. Karumanchi, E. P. Rhee, S. M. Parikh, PGC1α drives NAD biosynthesis linking oxidative metabolism to renal protection. *Nature* **531**, 528–532 (2016).
43. H. Shevalye, Y. Maksimchyk, P. Watcho, I. G. Obrosova, Poly(ADP-ribose) polymerase-1 (PARP-1) gene deficiency alleviates diabetic kidney disease. *Biochim. Biophys. Acta* **1802**, 1020–1027 (2010).
44. J. Zheng, K. Devalaraja-Narashimha, K. Singaravelu, B. J. Padanilam, Poly(ADP-ribose) polymerase-1 gene ablation protects mice from ischemic renal injury. *Am. J. Physiol. Renal Physiol.* **288**, F387–F398 (2005).
45. K. Ouararhni, R. Hadj-Slimane, S. Ait-Si-Ali, P. Robin, F. Mietton, A. Harel-Bellan, S. Dimitrov, A. Hamiche, The histone variant mH2A1.1 interferes with transcription by down-regulating PARP-1 enzymatic activity. *Genes Dev.* **20**, 3324–3336 (2006).
46. M. Peng, M. J. Falk, V. H. Haase, R. King, E. Polyak, M. Selak, M. Yudkoff, W. W. Hancock, R. Meade, R. Saiki, A. L. Lunceford, C. F. Clarke, D. L. Gasser, Primary coenzyme Q deficiency in *Pdss2* mutant mice causes isolated renal disease. *PLOS Genet.* **4**, e1000061 (2008).
47. Y. Qiu, X. Hu, C. Xu, C. Lu, R. Cao, Y. Xie, J. Yang, Ketogenic diet alleviates renal fibrosis in mice by enhancing fatty acid oxidation through the free fatty acid receptor 3 pathway. *Front. Nutr.* **10**, 1127845 (2023).
48. J. A. Torres, S. L. Kruger, C. Broderick, T. Amarlkhagva, S. Agrawal, J. R. Dodam, M. Mrug, L. A. Lyons, T. Weimbs, Ketosis ameliorates renal cyst growth in polycystic kidney disease. *Cell Metab.* **30**, 1007–1023.e5 (2019).
49. J. Rutkowska, E. T. Sadowska, M. Cichon, U. Bauchinger, Increased fat catabolism sustains water balance during fasting in zebra finches. *J. Exp. Biol.* **219**, 2623–2628 (2016).
50. Y. Takei, R. C. Bartolo, H. Fujihara, Y. Ueta, J. A. Donald, Water deprivation induces appetite and alters metabolic strategy in *Notomys alexis*: Unique mechanisms for water production in the desert. *Proc. Biol. Sci.* **279**, 2599–2608 (2012).
51. S. D. Morrison, A method for the calculation of metabolic water. *J. Physiol.* **122**, 399–402 (1953).
52. A. Wangsiripaisan, P. E. Gengaro, C. L. Edelstein, R. W. Schrier, Role of polymeric Tamm-Horsfall protein in cast formation: Oligosaccharide and tubular fluid ions. *Kidney Int.* **59**, 932–940 (2001).
53. H. Kaminski, L. Couzi, M. Eberl, Unconventional T cells and kidney disease. *Nat. Rev. Nephrol.* **17**, 795–813 (2021).
54. T. Ando, H. Wu, D. Watson, T. Hirano, H. Hirakata, M. Fujishima, J. F. Knight, Infiltration of canonical Vγ4/Vδ1 γδ T cells in an Adriamycin-induced progressive renal failure model. *J. Immunol.* **167**, 3740–3745 (2001).
55. S. Clotet-Freixas, O. Zaslaver, M. Kotlyar, C. Pastrello, A. T. Quaile, C. M. McEvoy, A. D. Saha, S. Farkona, A. Boshart, K. Zorcic, S. Neupane, K. Manion, M. Allen, M. Chan, X. Chen, A. P. Arnold, P. Sekula, I. Steinbrenner, A. Köttgen, A. B. Dart, B. Wicklow, J. M. McGavock, T. D. Blydt-Hansen, C. Barrios, M. Riera, M. J. Soler, A. Isenbrandt, J. Lamontagne-Proulx, S. Pradeloux, K. Coulombe, D. Soulet, S. Rajasekar, B. Zhang, R. John, A. Mehrotra, A. Gehring, M. Puhka, I. Jurisica, M. Woo, J. W. Scholey, H. Röst, A. Konvalinka, Sex differences in kidney metabolism may reflect sex-dependent outcomes in human diabetic kidney disease. *Sci. Transl. Med.* **16**, eabm2090 (2024).
56. S. Bajwa, A. Luebbe, N. D. N. Vo, E. M. Piskor, C. Kosan, G. Wolf, I. Loeffler, RAGE is a critical factor of sex-based differences in age-induced kidney damage. *Front. Physiol.* **14**, 1154551 (2023).
57. C. Podrini, A. Koffas, S. Choksh, M. Vinciguerra, C. J. Lelliott, J. K. White, H. A. Adissu, R. Williams, A. Greco, MacroH2A1 isoforms are associated with epigenetic markers for activation of lipogenic genes in fat-induced steatosis. *FASEB J.* **29**, 1676–1687 (2015).
58. V. Pazienza, C. Panebianco, F. Rappa, D. Memoli, M. Borghesan, S. Cannito, A. Oji, G. Mazza, D. Tamburrino, G. Fusai, R. Barone, G. Bolasco, F. Villarroya, J. Villarroya, K. Hatsuzawa, F. Cappello, R. Tarallo, T. Nakanishi, M. Vinciguerra, Histone macroH2A1.2 promotes metabolic health and leanness by inhibiting adipogenesis. *Epigenetics Chromatin* **9**, 45 (2016).
59. B. N. Finck, M. C. Gropler, Z. Chen, T. C. Leone, M. A. Croce, T. E. Harris, J. C. Lawrence, D. P. Kelly, Lipin 1 is an inducible amplifier of the hepatic PGC-1α/PPARα regulatory pathway. *Cell Metab.* **4**, 199–210 (2006).
60. Y. Wang, T. Nakajima, F. J. Gonzalez, N. Tanaka, PPARs as metabolic regulators in the liver: Lessons from liver-specific PPAR-null mice. *Int. J. Mol. Sci.* **21**, 2061 (2020).
61. K. Anastassiadis, J. Fu, C. Patsch, S. Hu, S. Weidlich, K. Duerschke, F. Buchholz, F. Edenhofer, A. F. Stewart, Dre recombinase, like Cre, is a highly efficient site-specific recombinase in *E. coli*, mammalian cells and mice. *Dis. Model. Mech.* **2**, 508–515 (2009).
62. J. P. Concordet, M. Haeussler, CRISPOR: Intuitive guide selection for CRISPR/Cas9 genome editing experiments and screens. *Nucleic Acids Res.* **46**, W242–W245 (2018).
63. R. Sebastian, E. K. Hosogane, E. G. Sun, A. D. Tran, W. C. Reinhold, S. Burkett, D. M. Sturgill, P. R. Gudla, Y. Pommier, M. I. Aladjem, P. Oberdoerffer, Epigenetic regulation of DNA repair pathway choice by MacroH2A1 splice variants ensures genome stability. *Mol. Cell* **79**, 836–845.e7 (2020).
64. D. C. Rogers, E. M. C. Fisher, S. D. M. Brown, J. Peters, A. J. Hunter, J. E. Martin, Behavioral and functional analysis of mouse phenotype: SHIRPA, a proposed protocol for comprehensive phenotype assessment. *Mamm. Genome* **8**, 711–713 (1997).
65. H. Fuchs, J. A. Aguilar-Pimentel, O. V. Amarie, L. Becker, J. Calzada-Wack, Y. L. Cho, L. Garrett, S. M. Hölter, M. Irmler, M. Kistler, M. Kraiger, P. Mayer-Kuckuk, K. Moreth, B. Rathkolb, J. Rozman, P. da Silva Buttkus, I. Treise, A. Zimprich, K. Gampe, C. Hutterer, C. Stöger, S. Leuchtenberger, H. Maier, M. Miller, A. Scheideler, M. Wu, J. Beckers, R. Bekeredjian, M. Brielmeier, D. H. Busch, M. Klingenspor, T. Klopstock, M. Ollert, C. Schmidt-Weber, T. Stöger, E. Wolf, W. Wurst, A. Ö. Yildirim, A. Zimmer, V. Gailus-Durner, M. Hrabě de Angelis, Understanding gene functions and disease mechanisms: Phenotyping pipelines in the German Mouse Clinic. *Behav. Brain Res.* **352**, 187–196 (2018).
66. V. Gailus-Durner, H. Fuchs, L. Becker, I. Bolle, M. Brielmeier, J. Calzada-Wack, R. Elvert, N. Ehrhardt, C. Dalke, T. J. Franz, E. Grundner-Culemann, S. Hammelbacher, S. M. Hölter, G. Hölzlwimmer, M. Horsch, A. Javaheri, S. Vetoslav Kalaydjiev, M. Klempt, E. Kling, S. Kunder, C. Lengger, T. Lisse, T. Mijalski, B. Naton, V. Pedersen, C. Prehn, G. Przemeck, I. Racz, C. Reinhard, P. Reitmeir, I. Schneider, A. Schrewe, R. Steinkamp, C. Zybill, J. Adamski, J. Beckers, H. Behrendt, J. Favor, J. Graw, G. Heldmaier, H. Höfler, B. Ivandic, H. Katus, P. Kirchhof, M. Klingenspor, T. Klopstock, A. Lengeling, W. Müller, F. Ohl, M. Ollert, L. Quintanilla-Martinez, J. Schmidt, H. Schulz, E. Wolf, W. Wurst, A. Zimmer, D. H. Busch, M. Hrabě de Angelis, Introducing the German Mouse Clinic: Open access platform for standardized phenotyping. *Nat. Methods* **2**, 403–404 (2005).
67. H. Fuchs, V. Gailus-Durner, T. Adler, J. A. Aguilar-Pimentel, L. Becker, J. Calzada-Wack, P. Da Silva-Buttkus, F. Neff, A. Götz, W. Hans, S. M. Hölter, M. Horsch, G. Kastenmüller, E. Kemter, C. Lengger, H. Maier, M. Matloka, G. Möller, B. Naton, C. Prehn, O. Puk, I. Rácz, B. Rathkolb, W. Römisch-Margl, J. Rozman, R. Wang-Sattler, A. Schrewe, C. Stöger, M. Tost, J. Adamski, B. Aigner, J. Beckers, H. Behrendt, D. H. Busch, I. Esposito, J. Graw, T. Illig, B. Ivandic, M. Klingenspor, T. Klopstock, E. Kremmer, M. Mempel, S. Neschen, M. Ollert, H. Schulz, K. Suhre, E. Wolf, W. Wurst, A. Zimmer, M. Hrabě de Angelis, Mouse phenotyping. *Methods* **53**, 120–135 (2011).
68. B. Rathkolb, W. Hans, C. Prehn, H. Fuchs, V. Gailus-Durner, B. Aigner, J. Adamski, E. Wolf, M. Hrabě de Angelis, Clinical chemistry and other laboratory tests on mouse plasma or serum. *Curr. Protoc. Mouse Biol.* **3**, 69–100 (2013).
69. J. Rozman, B. Rathkolb, S. Neschen, H. Fuchs, V. Gailus-Durner, M. Klingenspor, E. Wolf, M. Hrabě de Angelis, Glucose tolerance tests for systematic screening of glucose homeostasis in mice. *Curr. Protoc. Mouse Biol.* **5**, 65–84 (2015).
70. J. Rozman, M. Klingenspor, M. Hrabě de Angelis, A review of standardized metabolic phenotyping of animal models. *Mamm. Genome* **25**, 497–507 (2014).
71. K. N. Frayn, Calculation of substrate oxidation rates in vivo from gaseous exchange. *J. Appl. Physiol.* **121**, 628–634 (1983).
72. A. Dobin, C. A. Davis, F. Schlesinger, J. Drenkow, C. Zaleski, S. Jha, P. Batut, M. Chaisson, T. R. Gingeras, STAR: Ultrafast universal RNA-seq aligner. *Bioinformatics* **29**, 15–21 (2013).
73. Y. Liao, G. K. Smyth, W. Shi, FeatureCounts: An efficient general purpose program for assigning sequence reads to genomic features. *Bioinformatics* **30**, 923–930 (2014).
74. M. I. Love, W. Huber, S. Anders, Moderated estimation of fold change and dispersion for RNA-seq data with DESeq2. *Genome Biol.* **15**, 550 (2014).
75. F. Supek, M. Bošnjak, N. Škunca, T. Šmuc, Revigo summarizes and visualizes long lists of gene ontology terms. *PLOS ONE* **6**, e21800 (2011).
76. L. Recoules, A. Heurteau, F. Raynal, N. Karasu, F. Moutahir, F. Bejjani, I. Jariel-Encontre, O. Cuvier, T. Sexton, A. C. Lavigne, K. Bystricky, The histone variant macroH2A1.1 regulates RNA polymerase II-paused genes within defined chromatin interaction landscapes. *J. Cell Sci.* **135**, jcs259456 (2022).
77. M. Buschbeck, I. Uribesalgo, I. Wibowo, P. Rué, D. Martin, A. Gutierrez, L. Morey, R. Guigó, H. López-Schier, L. Di Croce, The histone variant macroH2A is an epigenetic regulator of key developmental genes. *Nat. Struct. Mol. Biol.* **16**, 1074–1079 (2009).
78. J. Douet, D. Corujo, R. Malinverni, J. Renauld, V. Sansoni, M. P. Marjanović, N. Cantariño, V. Valero, F. Mongelard, P. Bouvet, A. Imhof, M. Thiry, M. Buschbeck, MacroH2A histone variants maintain nuclear organization and heterochromatin architecture. *J. Cell Sci.* **130**, 1570–1582 (2017).

Acknowledgments: We thank all members of the Buschbeck laboratory, especially V. Valero and A. Pérez for technical support, as well as I. Guberovic and S. Hurtado-Bagès for discussions. We also thank Ó. Yanes, S. Abelló, and A. Junza from the Metabolomics Platform at Universitat

Rovira i Virgili, Tarragona, Spain, for performing metabolomics experiments. At Helmholtz Munich, we acknowledge the help of S. Pai and the expert technical support of our technicians and the Core Facility Laboratory Animal Services. **Funding:** This study has been supported by the national grant PID2021-126907NB-I00 from MCIN/AEI/10.13039/501100011033, cofunded by European Regional Development Fund (ERDF; a way of making Europe) to M.B. R.W. was partially funded by a Walter Benjamin postdoctoral fellowship from the German Research Foundation (DFG; project 498523371). Research in the Buschbeck laboratory is further supported by the following grants: the Marie Skłodowska Curie Training Network "INTERCEPT-MDS" (H2020-MSCA-ITN-2020-953407), the Marie Skłodowska Curie Doctoral Network "NUCLEAR" (HORIZON-MSCA-2023-DN-101166838), LaCaixa Banking Foundation (CI24-10180), AGAUR 2021-SGR-260, and PRYGN222668BUSC from the Fundación AECC. Research at the IJC is supported by the Fundació Internacional Josep Carreras and the CERCA Programme/Generalitat de Catalunya. This work was supported by the German Federal Ministry of Education and Research (INFRAFRONTIER grant 01KX1012 to M.H.d.A.) and the German Center for Diabetes Research (DZD; to M.H.d.A. and R.T.). P.O. received support from the National Institutes of Health (NIH) through grants from the National Institute of General Medical Sciences (R35GM153484) and the National Cancer Institute (NCI; R01CA285725). E.B. received support through grant NIH/NCI R01CA154683. **Author contributions:** Conceptualization: M.H.d.A., R.T., and M.B. Data curation: R.W., A.S.-M., J.C.-W., B.R., N.R.V.D., R.G., J.R., A.A.-P., and L.B. Formal analysis: R.W., N.R.V.D., A.S.-M., A.A.-P., and L.B. Funding acquisition: M.H.d.A., R.T., and M.B. Investigation: R.W., G.C.-A., D.C., A.S.-M., J.C.-W., S.A.B., B.R., N.R.V.D., V.C., M.R.D., R.G., J.R., T.K.-R., A.A.-P., L.B., C.S., and S.M. Project administration: H.F., V.G.-D., R.T., and M.B. Methodology: R.W., G.C.-A., D.C., A.S.-M., J.C.-W., S.A.B., B.R., N.R.V.D., R.G., J.R., T.K.-R., A.A.-P., L.B., C.S., and S.M. Resources: C.X.Q., V.C., D.F., D.H.P., M.R.D., V.K.C., E.B., M.V., P.O., and M.B. Software: D.C. and S.A.B. Supervision: H.F., V.G.-D., R.T., and M.B. Validation: R.W. Visualization: R.W. and D.C. Writing—original draft: R.W., R.T., and M.B. Writing—review and editing: R.W., R.T., and M.B. **Competing interests:** The authors declare that they have no competing interests. **Data and materials availability:** All data needed to evaluate the conclusions in the paper are present in the paper and/or the Supplementary Materials. The RNA-seq data generated and analyzed for this study have been deposited in the Gene Expression Omnibus database under accession number GSE254938 (www.ncbi.nlm.nih.gov/geo/query/acc.cgi?acc=GSE254938). The *Macroh2a1* KO mouse line can be shared with interested scientists based on double signed collaboration agreements. Specific terms will be decided based on scientific and/or commercial interests of the collaboration partner. The *Macroh2a2* KO mouse line was generated for the IMPC and can be ordered from EMMA (European Mouse Mutant Archive) under EM:13630. The macroH2A1.2/macroH2A2 DKO mouse line can be provided by P.O. pending scientific review and a completed material transfer agreement with Johns Hopkins University, School of Medicine, Baltimore, USA. Requests for the macroH2A1.2/macroH2A2 DKO mouse line should be directly submitted to po@jhmi.edu.

Submitted 19 May 2025
Accepted 22 September 2025
Published 24 October 2025
10.1126/sciadv.adz1242